A Study on the tunnel barrier in a top-gated Si/SiGe quantum device

By

Hyuncheol Shin

A dissertation submitted in partial fulfillment of

the requirements for the degree of

Doctor of Philosophy

(Electrical Engineering)

at the

UNIVERSITY OF WISCONSIN-MADISON

2012

Date of final oral examination: 06/11/12

The dissertation is approved by the following members of the Final Oral Committee:

Robert H. Blick. Professor, Electrical Engineering

Luke J. Mawst, Professor, Electrical Engineering

Zhenqiang (Jack) Ma, Professor, Electrical Engineering

Mark A. Eriksson, Professor, Physics

Susan Coppersmith, Professor, Physics

Acknowledgements

I would have not been able to come to the end without great supports from many people. I would like to show my deep appreciations to those people who helped me to complete my thesis research.

First of all, I thank Professor Robert Blick for serving as my Ph.D advisor. His ‘opened-door lab’ policy really opens up the opportunities for ‘whoever’ wants to achieve what they want to, in his group. He never judged students based on intellectual ability; rather he cared about passion, taking ownership and challenges. One day, he said to me that my job is just finding problems, but finding solutions. His comment changed my attitude. I was worrying too much about roadblocks on the way. Now, I realized that seeing the problems are OK, but I should rather enjoy the moments of tackling those problems to achieve the goal, than being afraid of failure. Indeed, as the current President of South Korea, Lee, said, Trying and failing is better than not trying and not failing. Having spent 7 years with him, I am feeling empowered to do something challenging.

I thank Professor Mark Eriksson for his financial and academic support in my research. I was also lucky that I had an opportunity to work in the silicon quantum computing group, which is one of the greatest research communities I’ve ever seen, which is built by his brilliant management skill. Without his financial support, I would have not been able to set up the Dilution fridge. Also, he was very knowledgeable and instructive educator. I’ve learned a lot about low temperature measurements and physics

in my research subject. He showed me how to achieve something in a systemic way. He also showed me how to collaborate with other people respectfully. He was always generous, and kind to me.

I thank Dr. Mark Friesen for endless discussions on modeling work and the theoretical background. Mark's door was always open, and his personality made me feel so comfortable to talk anything about I don't understand. Without his support, my simulation should have taken more than a year. I thank Professor Susan Coppersmith. Sue inspired me to come up with models that I've developed. She did not interfere much as a big guy, but she always suggests a big picture.

I thank many people around my lab., I thank Chulki. We shared our Ph.D life as the best friend each other in Madison. He also motivated me in terms of being a good researcher. I thank Hyunseok who guided my as the senior Korean student when I first joined the group. I thank Hua for sharing his experience and giving me directions as senior post Doc. in the group. I thank Nakul for sharing his knowledge in quantum dot as the senior student in the quantum computing project. I thank all other people in the lab. who helped and worked together each other. These people include Jonghoo, Hyuncheol, Eric, Abhishek and Changyang as well as other colleagues in the lab. I specially thank Dustin. He and I had worked so hard to set up the new lab. in ME1166B. I will never forget the moments that he and I have spent in the lab. I thank Madhu, Christie and Jonathan in Mark Eriksson's lab. for sharing their experience and knowledge on fridge management and quantum dot experiment.

I thank my parents and my brother and sister. Their love made me not to give up during the hard time. They are the pillars of my life. My father and mother continuously pray for me which becomes the great encouragement when I encounter a difficulty. I love you mother and father.

Last, but not the least, I thank to my wife, Yoonsun Lee. She and I have gone through the life in Madison together. We shared our fun moments, challenging moments, and sad moments. Without her love and support, I certainly would have not been able to finish my degree. Also, my life in Madison would have been extremely cold as the weather gets in the winter. I love you honey, I will never stop loving you.

I thank God. In him, every moment in my life becomes meaningful. Believing in him, I was able to make decision to study abroad 7 years ago. I pray that I would become a man that he wants to be, and use my talent for his purpose.

Table of Contents

Acknowledgements iii

List of Figures vi

List of Tables viii

Chapter 1: Introduction 1

1.1 Quantum computing 1

1.2 Semiconductor quantum dots as an electron spin qubit 2

1.3 Tunnel barriers in semiconductor quantum dots 6

1.4 Organization of the thesis 8

Chapter 2: Two-dimensional Electron Gas in Si/SiGe Heterostructures 9

2.1 Introduction 9

2.2 Si/SiGe Heterostructures 10

2.3 Electrical Characterization of the 2DEG 13

2.3.1 Mobility and Carrier density 15

2.3.2 Carrier Lifetimes 19

Chapter 3: Device fabrication and Low temperature measurement set-up 23

3.1 Introduction 23

3.2 Device design and fabrication 24

3.3 Low temperature set-up 30

Chapter 4: Tunnel barrier in a top-gated Si/SiGe quantum device 37

4.1 Introduction 37

4.2 Experiments 38

4.3 Two-dimensional modeling 45

4.3.1 Infinite barrier models...47

4.3.2 Finite barrier models 55

4.4. Effective 1D barriers..59

Chapter 5: Conclusions 67

5.1 Comparison of effective lengths of the barriers 67

5.2 Energy dependence of the tunneling conductance 68

Appendix A: Electromagnetic field noise measurement in ME1166B........................71

Appendix B: Vibration measurement in ME1166B...85

Appendix C: Tunneling in a 1D rectangular barrier 88

Appendix D: Table of parametric equations used in the models 98

Bibliography 99

List of Figures

Figure 1.1: Top gated semiconductor heterostructure quantum dots. 4

Figure 2.1: Schematic diagram of a Si/SiGe Heterostructure used in the experiment. 11

Figure 2.2: Hall measurement. 14

Figure 2.3: SDH oscillations and dingle plot to determine quantum lifetime. 21

Figure 3.1: Fabrication flow of HallDot device. 26

Figure 3.2: Pictures of HallDot chip 27

Figure 3.5: Phase diagram of ^{3}He – ^{4}He 31

Figure 3.6: Dilution refrigerator and its schematic diagram showing flow of ^{3}He............32

Figure 3.8: The tailpiece 35

Figure 4.1: A scanning electron microscope images of the gate geometry identical to the one used in the experiments. 39

Figure 4.2: Measurement circuit and the pinch off characteristic of the top gate pair 40

Figure 4.3: Temperature dependence of tunneling conductance & activation energy 42

Figure 4.4: Illustration of the two infinite 2D barrier models..48

Figure 4.5: Flow chart of parameterization procedure for IC model 49

Figure 4.6: Fitting result of E_{w0} to E_a...51

Figure 4.7: Conductance data used for fitting *r* and fitting result. 52

Figure 4.8: Conductance fitting result for IC model 53

Figure 4.9: Fitting results for IR model 54

Figure 4.10: Illustration of the two Finite 2D barrier models developed in the work. 56

Figure 4.12: Illustrations of how to extract effective 1D barriers from the 2D models. ...62

Figure 4.13: Effective 1D barriers extracted from the 2D models. 63

Figure 4.14: Comparison of effective 1D effective barrier length, L_b extracted 64

Figure 4.15: Fractional change of tunneling conductance as a function of energy 69

Figure A.1: WiFi Antenna locations..75

Figure A.2: EMF levels from WiFi Antenna locations...76

Figure A.3: The schematic view and distribution of electric field inside the lab with MacBook Wi-Fi on/off. 77

Figure A.5: Electric field time dependence at location A and B... 80

Figure A.6: Fitting of the EMF distribution data measured...81

Figure A.7: Fitting of the EMF distribution data measured (blue dots) in the lab to the Gaussian distribution function 83

Figure C.1: A 1D rectangular potential barrier located at x = 0 89

Figure C.2: A 1D rectangular potential barrier located at x = -a/2. 94

List of Tables

Table 2.1: Carrier densities and motilities calculated from SDH oscillations 18

Table 4.1: Energy dependent coefficient, E_i, for each model 70

Table B.1: Vibration measurement results...81

Chapter 1

Introduction

1.1 Quantum Computing

We live in the information age, with a flood of information and cutting edge technology to deal with it. Computers are the core equipment to process information and the computing technology has been evolved dramatically to match the growth of our necessity. However, the most fundamental technology has not been changed since the invention of the computer, which is using classical bit "0" and "1". CMOS technology became industry standard to realize the classical bit using the voltages of a transistor [1]. Physics involved in such transistors is based on classical diffusive transport. Current scaling technology brought down the device scale to 22nm [2], and it will eventually become comparable with Fermi wavelength of electrons as further scaling down. At that point, we should treat the transport quantum mechanically.

Quantum computing has been suggested to overcome the limitation of the classical computer. Analogous to the classical computer, quantum computing also uses binary information, and the unit of the information in quantum computer is called "qubit"

as corresponding to the classical bit. Quantum mechanics is the governing physics, which make the qubit characteristics completely different than classical bit. Two states of a qubit can be super positioned (both states can be expressed simultaneously) and they are entangled. These characteristics may sound disruptive for classical information process. However, computing becomes much more powerful.

The power of the quantum computer can be easily seen in quantum parallism. In classical computers, parallel computing is performed by putting multiple processors linked parallel. Each processor performs one at the same time. In a quantum computer, a single quantum processor can perform multiple computations by utilizing superposition-ability. The power of quantum computer grows exponentially as number of bit increases. With the progress in development of quantum algorithms such as Shor's algorithm for integer factorization [3], quantum computing concept has drawn more and more attentions these days.

1.2 Semiconductor quantum dot as a electron spin qubit

In principle, any quantum two level systems can be a qubit. DiVincenzo suggested five criteria for the implementation of a quantum computer [4]. Those criteria are listed:

1. A scalable physical system with well-defined qubits.
2. Ability to be initializable to a simple fiducially state such as $|000....\rangle$
3. Longer coherence times than gate operation times.
4. A universal set of quantum gates.
5. Qubit-specific measurements.

There are many candidates for physical implementation of qubits ranging from natural atoms to superconductors. In this research, we focus on single electron spin in semiconductor quantum dots. It is first proposed by Loss and DiVincenzo in 1998 [5]. Using semiconductor has some advantages including scalability, and compatibility with conventional CMOS technology. However, there are usually so many electrons in semiconductors. To use single spin as a qubit, single electron has to be isolated from other. In Loss and DiVincenzo's proposal, electrons are confined in three dimensional potential wells or "quantum dots". Firstly, electrons are confined in very thin two dimensional quantum well created by heterostructure growth. Now, electrons are confined in vertical direction, z, but still free to move along x, y directions (Such two dimensional electronic system in semiconductor heterostructures is called 2DEG (Two Dimensional Electron Gas) will be discussed in chapter 2). Lithographically defined nano-scale gates on top of the surface are used to give lateral confinements using negative bias. When negative voltages are applied on nano gates, electrons underneath the gates are depleted, and potential barriers are created. The more the negative gate

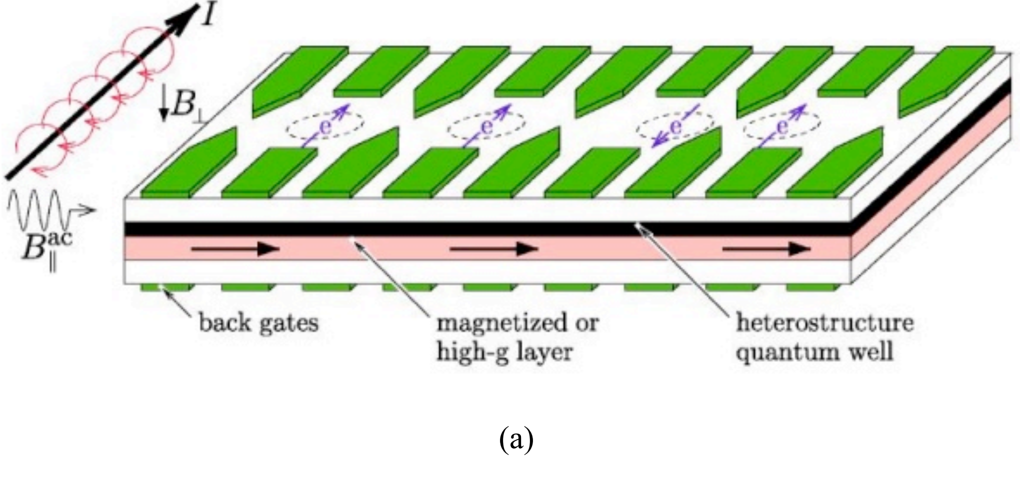

(a)

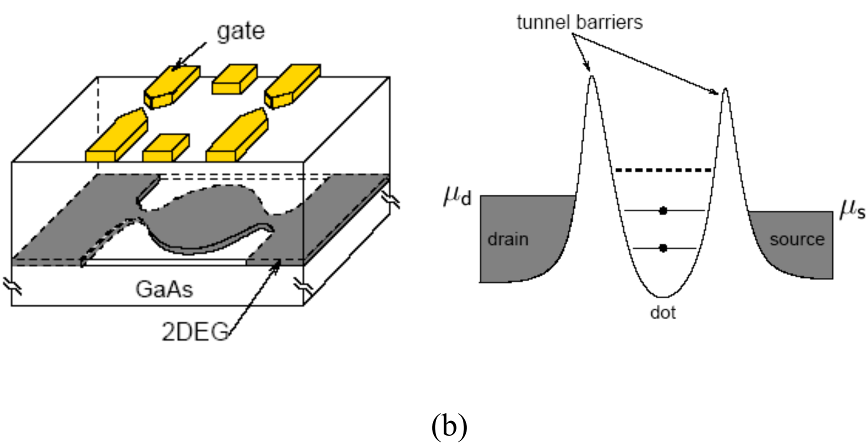

(b)

Figure 1.1: Top gated semiconductor heterostructure quantum dots. (a) Illustration of single electron spin qubit proposal similar to [5] using two external magnetic fields, $B_\perp$ and B^{ac}. (b) Depletion of 2DEG underneath the top-gates due to negative gate voltage (right), and resulting one-dimensional potential profile showing tunnel barriers and the quantum dot (left).

voltage will form the higher and wider potential barriers. In principle, single electron can be confined using this approach. The magnetic moment associated with the electron spin is tiny and therefore hard to measure directly. To establish well defined two level system, spin up and down states are splitted by Zeeman splitting using perpendicular magnetic field, $B_{\perp}$. By correlating the spin states to different charge states , and subsequently measuring the charge on the dot, the spin state can be determined. This is called spin-to - charge conversion. Spin control is performed by AC magnetic field, B^{ac} using electron spin resonance. A conceptual cartoon of such electron spin qubit using top gated semiconductor heterostructure quantum dots is shown in Figure 1.1(a).

In Figure 1.1(b), a conceptual diagram of one-dimensional potential landscape of such semiconductor quantum dots is shown (right). As explained earlier, the tunnel barriers are gate controlled. As the size of the quantum well, or "dot" between the barrier becomes comparable with Fermi wavelength of the electron, discrete energy levels are formed inside the dot. This is much like an atom with discrete orbital states, so semiconductor quantum dots are often called "artificial atom".

1.3 Tunnel barriers in semiconductor quantum dots

Gate controlled potential barriers are the fundamental building blocks of the semiconductor quantum dots qubit [5,6]. They determine electron occupation in a dot and the energy scales inside the dot. They also play a critical role in time domain study of a quantum dot, such as observation of coherence of electron charge and spin states [7], and spin read out using pulsed gate single-shot measurement utilizing spin-to-charge conversion and energy dependent tunneling [8, 9].

For those time domain studies, energy dependent tunneling is utilized. Basically, an electron with higher energy tunnels in/out faster than one with lower energy. K. MacLean studied energy dependence of tunnel rates in a GaAs quantum dot, showing exponential dependence of the rates on drain-source bias and plunger gate voltages [10]. In silicon, the effects of energy dependent tunneling are expected to be enhanced compared to GaAs, because of the carriers' larger effective mass. In Si/SiGe quantum dots, energy dependent tunneling have been studied and utilized in studying dot system such as spin relaxation time (T_1) measurement and excited state spectroscopy [11-14].

There have been only a few studies in energy dependent tunneling in top-gated quantum dot devices. Also there have not been much study on the tunnel barrier itself. Understanding the barrier inforamtion such as height, width, and shape of the barrier is important, because it determine the level of the energy dependence of the tunnel rates. Understanding energy dependence of the tunnel rates is critical in qubit operation because

many spin measurement including single-shot readout utilizes the energy dependent tunneling.

The motivation of the research in the thesis is to study the tunnel barrier in our top gated Si/SiGe quantum devices, so that we understand better how the shape of the barrier in our dot system look like, and how it affects to the conductance. We hope that we can use the barrier information as an important background knowledge in studying qubit operation. To study the barrier, we should have a proper model. The tunnel barries are often modeled as 1D, just like the one shoen in Figure 1.1(b). Recently, Mark Friesen suggested that the tunnel barrier should be treated as two dimensional (2D), since wavefunctions in the tunnel gap spread in nontrivial fashion into higher dimensions [15].

We study the barrier both experimentally and theoretically. We measured tunneling conductance as functions of drain-source bias, gate voltage and temperature. We also developed empirical 2D models that fits experimental conductance. We utilize theory developed in [15] for numerical calculation of conductance in the developed models.

1.7 Organization of thesis

The organization of the thesis is following. In chapter one, background knowledge on electron spin quantum computing using semiconductor quantum dots is introduced first. Then, the motivation of the research and the organization of the thesis are stated. In chapter two, material design and electrical characterization is discussed. I will introduce 2DEG in Si/SiGe heterostructure used in the research and talk about how to determine carrier density, mobility and life times of carriers from low temperature Hall measurement. In chapter three, device design and fabrication is introduced as well as low temperature measurement set up used in the experiment. In chapter four, tunneling measurement and two dimensional modeling works are discussed, starting from brief introduction of transfer matrix method to calculate transmission coefficient in a one dimension rectangular barrier. Finally, in chapter five, I will give conclusion of the research.

Chapter 2

Two-dimensional Electron Gas in Si/SiGe Heterostructures

2.1 Introduction

A semiconductor heterostructure consists of at least two different materials with different bandgap. It allows bandgap engineering to modify electronic property of a bulk semiconductor, leading to many practical inventions, including semiconductor lasers, photo voltaic devices and high electron mobility transistors (HEMT). In 2000, two scientists are awarded the Nobel Prize in physics for developing semiconductor heterostructures used in high-speed- and opto-electronics [16]. Not only the industrial impact, semiconductor heterostructure 2DEG is widely used in academic research in studying electron transport in semiconductors because the mobility is so high that the momentum of the electrons are preserved without scattering for longer distance than bulk. In this chapter, I will talk about the Si/SiGe heterostructure for 2DEG. In 2.1 I will talk about epitaxial layer structure of the heterostructure and how a 2DEG is formed in such heterostructures. Then, I will discuss about low temperature electrical characterization of

the 2DEG used in the research. In 3.2.1, I will talk about mobility and carrier density. In 3.2.2, I will discuss about carrier lifetimes that are determined from dingle plots, which tells us what the dominant scattering mechanism is in the material.

2.2 Si/SiGe Heterostructures

A semiconductor 2DEG is a sheet of electrons confined in the potential well formed in the conduction band of a heterostructure. While GaAs/AlGaAs heterostructures are the most widely used material system for making semiconductor 2DEG, due to small lattice mismatch, which allows more freedom in bandgap engineering. Silicon based heterostructures also have drawn much attentions due to many advantages including compatibility with the conventional silicon electronics. The obvious advantages of Si/SiGe heterostructures were recognized at an early stage of research, with the first report on a Si/SiGe superlattice appearing already back in 1975[17]. After more than 30 years of research and development in this field, SiGe is now used in CMOS transistors as a strain-inducing layer.

One of the challenges in Si/SiGe is a large lattice mismatch. Silicon and germanium have mismatch amounts to 4.2%. So, it requires more careful material design to adjust the amount of strain. Here, I will discuss how a 2DEG is formed using the layer structure of a typical Si/SiGe heterostructure used in the research shown in Figure 2.1.

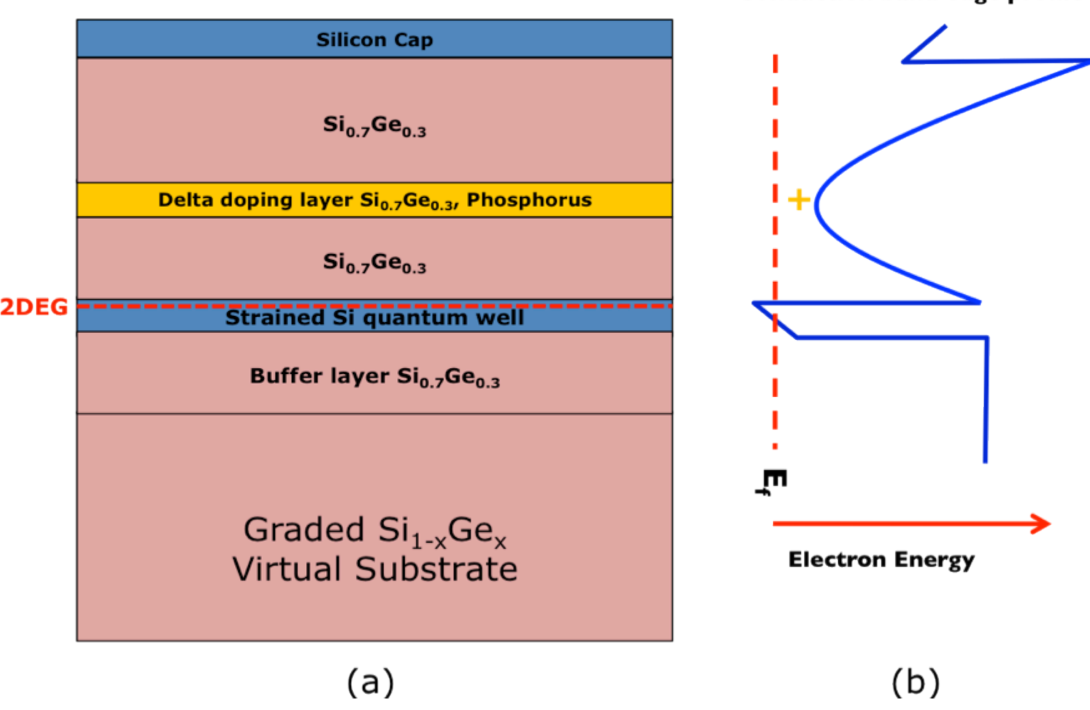

Figure 2.1: Schematic diagram of a typical Si/SiGe Heterostructure used in the experiment. (a) Layer sequence (b) Schematic of conduction band edge profile of the structure shown in (a)

The heterostructures used in this research were grown using chemical vapor deposition (CVD) Dr. Don Savage at the Material Science Program of the University of Wisconsin Madison. Starting from the bottom, $Si_{0.7}SiGe_{0.3}$ virtual substrate is grown on top of a silicon substrate, where germanium composition is linearly increased from 0% to 30% to adjust the strain. The grading is ~2.4% per step with each step ~233nm thick. Then 1μm

of buffer layer with constant germanium composition of 30% is grown. The advantage of this double layer approach to relax strain is that the misfit dislocations are distributed over the thickness of the buffer layer instead of being crowded into the interface plane, allowing most of the dislocations to propagate unaffected with a velocity determined by the growth temperature [18-20]. After adjust and relax the strain, the 10nm to 18nm of silicon quantum well layer is grown, sandwiched between buffer layer and the spacer layer of ~ 24nm thick $Si_{0.7}SiGe_{0.3}$. Due to the lattice mismatch, the silicon quantum well layer is tensile strained. The 2DEG is formed at the interface between un-doped silicon quantum well layer and spacer layer, where potential barrier is formed by conduction band offset. The amount of the band offset depends on the germanium composition [21]. In $Si_{0.7}SiGe_{0.3}$, the offset is ~150meV [21]. To supply electrons into the well, very thin and highly doped layer-delta doping layer-is grown. The reason why putting spacer later between the delta doping layer and the un-doped quantum well layer is to avoid impurity scattering, which is the dominant scattering mechanism in this kind of heterostructure at a low temperature where phonon scattering is absence. This technique is called "Modulation doping". Modulation-doped structure was first conceived by Dingle in 1978[22]. Due to the separation of the doping layer from the channel, the mobility of such modulation-doped heterostructures is greatly enhanced. Typical mobility for our 2DEG is an order of 100,000cm^2/Vs. The best mobility in Si/SiGe heterostructure reported is $1.6\times10^6 cm^2$/Vs in gate voltage induced 2DEG in an un-doped structure [23].

2.3 Electrical Characterization of the 2DEG

When the heterostructures are given, Low temperature Hall measurement was performed for electrical characterization. Low temperature Hall mobility is a great figure of merit to check the overall quality of a 2DEG. For sample preparation, Hall bars are defined by plasma etching using CF4 and ohmic contact is made with Au/Sb/Au layers followed by annealing at 400°C. A typical hall bar that is used in the study is shown In Figure 2.2 (a). Usually the Hall measurement was performed at the Mark Eriksson group using PPMS (Physical property measurement system) which has base temperature of 1.2K, equipped with the superconductor magnet witch goes up to 12Tesla. 1.2K is sufficient enough to observe quantum Hall effect which is an evidence of a 2DEG being formed. I will discuss the mobility and carrier density calculation in the following sub-section. The measurement was performed using PPMS at 1.7K. Detail of the low temperature measurement set up and measurement circuits can be found in chapter three of this thesis.

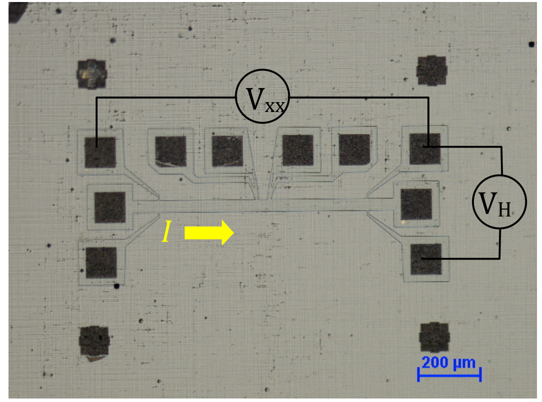

(a)

150
120
90
60
30
0
V[μV]
-8 -6 -4 -2 0 2 4 6 8
B[T]
V$_H$
V$_{xx}$

(b)

Figure 2.2: Hall measurement. (a) The optical microscopy image of a typical hall bar used in the experiment (current direction and voltage probes are indicated). (b) A typical longitudinal voltage V_{xx}, and transverse voltage, V_H measured from the Hall bar shown in (a) at 1.7K.

2.3.1 Mobility and Carrier density

In Figure 2.2 (b), measured longitudinal voltage, V_{xx} and transverse voltage, V_H (or Hall voltage) are shown. Carrier density, n_s and mobility, μ can be calculated from the transverse and longitudinal voltages at low magnetic field regime, where quantum Hall effect is not observed yet. In this regime, all you can see is the linear increase of the transverse voltage-Hall voltage, V_H as magnetic field increases. Carrier density is inversely proportional to Hall voltage, and directly measured from the slope of the Hall voltage with respect to the applied magnetic field.

$$n_s = \left[e \frac{d\rho_{yx}}{dB} \right]^{-1} = \frac{I/e}{dV_H/dB} \tag{2.1}$$

Here, ρ_{xy} is the transverse resistivity. e is electron charge, B is applied magnetic field, and I is the current flown in the hall bar. Once the carrier density is calculated, mobility can be calculated.

$$\mu = \frac{1}{en_s\rho_{xx}} = \frac{I/e}{n_s V_{xx} W/L} \tag{2.2}$$

ρ_{xx} is the longitudinal resistivity calculated from the measured V_{xx}. *W* and *L* are the width and the length of the Hall bar. Right hand side of (2-1) and (2-2) are all measured value of V_H or V_{xx}, geometry of the Hall bar, and bias current.

Now, in high field regime, quantum hall effect is observed in V_H. Quantum Hall effect is the quantization of hall resistance. It is first observed from the inversion layer of silicon MOSFET device [24]. The origin of the quantized hall effect is formation of Landau level. In V_{xx}, oscillations are observed, which is referred to as Shubnikov-deHass(SDH) oscillation. This is not unique to 2D conductors, and was first observed in bulk metals in 1930. However, in 2-D semiconductors the effect is much larger. The SDH oscillation is very useful to determine low temperature carrier density. Even if I can calculate it from low field result, I used SDH oscillations instead. Indeed, all the carrier density values in this thesis are actually calculated from SDH oscillation. Let me explain how I calculate carrier density as well as the detail of explain of the oscillations.

In 2-D system, the density of states is a step function. If temperature is significantly low, we consider only one subband.

$$N_s(E) = \frac{m}{\pi\hbar}\delta(E - E_s) \tag{2-3}$$

When magnetic field is applied, the density of states breaks up into a sequence of peaks spaced by $\hbar\omega_c$, where $\omega_c = eB/m$ is the cyclotron frequency

$$N_s(E,B) \approx \frac{2eB}{h}\sum_{n=0}^{\infty}\delta\left[E - E_s - (n+1/2)\hbar\omega_c\right] \quad (2\text{-}4)$$

These are called Landau levels. As magnetic field changes, the energies of Landau levels changes. The longitudinal conductivity is maximum when the Fermi energy lies at the center of a Landau level, and minimum when the Fermi energy lies between two Landau levels, and the conductivity goes through one cycle of oscillation. Because each Landau levels contain same number of states, we can calculate the number of occupied Landau levels simply by dividing ns by 2eB/h. Hence the magnetic field values B1 and B2 corresponding to two successive peaks must be related by

$$\frac{n_s}{2eB_1/h} - \frac{n_s}{2eB_2/h} = 1 \quad (2\text{-}5)$$

From here, we can calculate the carrier density

$$n_s = \frac{2e}{h}\frac{1}{(1/B_1) - (1/B_2)} \quad (2\text{-}6)$$

HeterostructureID	Hall bar ID	Mobility [cm^2/Vs]	Carrier density [$10^{11}/cm^2$]	Rs [Ω/cm^2]
09061501	1	129000	5.11	93
	2	145000	5.12	84
	3	133000	5.19	87
09080401	1	116000	4.46	140
	2	105000	4.29	149
	3	97400	4.17	149

Table 2.1: Carrier densities and motilities calculated from SDH oscillations. Six Hall bars from two different heterostructures are tested

In table 2.1, calculated carrier density and the mobility from the longitudinal voltage measurement that is similar to the data shown in Figure 2.2 (b) are shown. At that specific time, total six Hall bars from two chips were measured. At the first column, the heterostructure IDs are shown. “09061501” is grown on top of the virtual substrate made in the University of Wisconsin Madison. For “09080401”, the commercial virtual substrate from the company IQE is used. Second column is Hall bar ID. For each heterostructure, three Hall bars are tested, which are from the 4x4mm size chip (there are 4 Hall bars in each chip). The 2DEG is very homogeneous over the chip. As shown in the table 2.1, all of the three Hall bars from the same chip show very similar mobility and carrier density.

2.3.2 Carrier Lifetimes

Two characteristic carrier lifetimes have been determined from mobility and the SDH oscillation data, and compared to analyze quality of the heterostructure. In the transport theory of normal metallic systems, there are two different characteristic times - a single particle relaxation time τ_s, and a scattering time τ_t. They are also referred as a quantum lifetime and a transport lifetime. A single particle relaxation time describes the decay time of one-particle excitations and characterizing the quantum-mechanical broadening of the single-particle electron state by

$$\Gamma_s=\hbar/2\tau_s \tag{2-7}$$

and a scattering time is related to the DC conductivity by

$$\sigma = n_s e^2 \tau_t/m^* \tag{2-8}$$

[25]. From (2-8), the scattering time, τ_t is directly calculated with measured mobility and the carrier density. In the transport, scattering time is the characteristic time scale for carriers. It does not include small angle scatterings, because those small angle scatterings do not contribute to the transport. Even if electrons are scattered, if they made the transport, it contribute to the conductance. This is shown in (2-9).

$$\frac{1}{\tau_t} = \frac{m^*}{\pi\hbar^3}\int_0^{\pi} d\theta |V(q)|^2 (1-\cos\theta) \tag{2-9}$$

$$\frac{1}{\tau_q} = \frac{m^*}{\pi\hbar^3}\int_0^{\pi} d\theta |V(q)|^2 \tag{2-10}$$

V(q) is proportional to probability of scattering at a momentum *q*. The only difference between (2-9) and (2-10) is the cosine factor that eliminates contribution of small angle scatterings in (2-9). The ratio of τ_t and τ_q, which is called "Dingle ratio" reflects the dominant scattering mechanism (small angle scattering for a large ratio, large angle scattering for a ratio close to unity) [26].

Dingle ratio is useful measure of the quality of a 2DEG. In modulation-doped heterostructures, the dominant scattering mechanism is the long-range potential associated with ionized dopants, which are far from the 2DEG, and produce predominantly small angle scattering [27]. Therefore, we expect a large ratio for a high mobility 2DEG. In Si/SiGe 2DEG, the ratio of 22 was reported by K. Ismail et al which is from MBE grown heterostructure [28].

To measure the dingle ratio, quantum lifetime has to be determined. This is done by dingle plot, which is the logarithm plot of the amplitude of the SDH oscillations as a function of inverse of magnetic field.

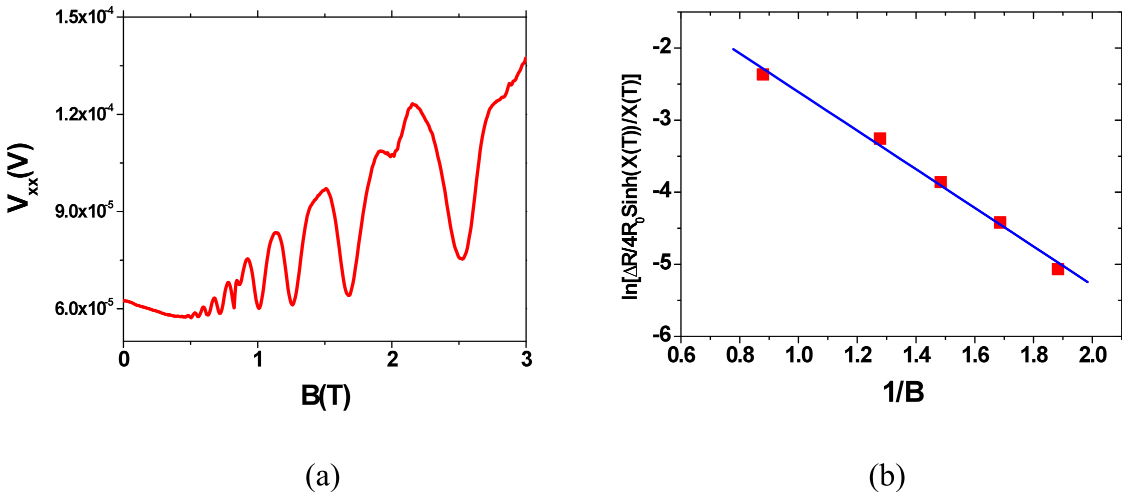

Figure 2.3: SDH oscillations and dingle plot to determine quantum lifetime.
(a) SDH oscillations measured at 60mK. (b) Dingle plot of (a), $\boldsymbol{\tau_q} =$ ~1.1ps

The amplitude ΔR is given by,

$$\Delta R = 4R_0 X(T)\exp(-\pi / \omega_c \tau_q) \qquad \text{(2-11)}$$

where, R_0 is the zero-field resistance, ω_c the cyclotron frequency, and $X(T)$, a thermal damping factor is given by

$$X(T) = (2\pi^2 kT / \hbar\omega_c) / \sinh(\exp(2\pi^2 kT / \hbar\omega_c) \qquad \text{(2-12)}$$

If the logarithm of the amplitude is plotted against $1/B$, the slope gives $1/\tau_q$ directly with and intercept of $4R_0$.

Quantum lifetime and dingle ratio of our Si/SiGe heterostructures have been determined. For this, Hall measurement was done at the dilution refrigerator to observe sufficient number of SDH oscillations at low magnetic field. Figure 2.3 shows a typical SDH oscillations measured at 60mK and the dingle plot. Transport lifetime, quantum lifetime and dingle ratio determined from the plot are ~9.53ps, ~1.2ps and ~8.86 respectably. The ratio is significantly higher than unity, which implies that the dominant scattering mechanism in our material is the remote site impurity. The value is definitely lower than the reported value in [28]. However, in [28], the material was grown with MBE, which usually shows better quality than CVD grown material.

Chapter 3

Device fabrication and Low temperature measurement set-up

3.1 Introduction

Research in nano-scale semiconductor device sometimes requires advanced tools, such as electron beam lithography and cryogenic temperature measurement set-up. Below 1K is necessary to study tunneling in semiconductor quantum dots, because the typical barrier height of those dot systems in an operation regime is a few mili-electron volt, which is corresponding to a thermal energy of a few Kelvin.

Dilution refrigerators using Helium-3 (^{3}He) and Helium-4 (^{4}He) mixture is one of the most popular cryogenic temperature system for low temperature physics research. In this chapter, I will talk about device design and fabrication and Low temperature measurement set-up. First, I will talk about device design and fabrication including a few improvement and trouble shootings in 3.2. In 3.3, I will talk about low temperature measurement set-up.

3.2 Device design and fabrication

Most of the sample fabrication process had been set up already, when I joined the group, so there was not much needs to develop the whole process to fabricate the quantum dots. While keeping the previously developed process recipe, I improved layout design to integrate Hall bar chip and quantum dot chip, which I call it "HallDot" design. Previously, Hall bar chips and quantum dot chips are fabricated separately. So, one had to fabricate two chips - one for material characterization, and the other one for device experiments. However, I found that quantum dots could be integrated on top of the hall bar chip. The integrated HallDot design not only save times and reduces fabrication cost, it also has other benefits such as pre-screening of the bad patterns. In the following, I will talk about the detail of the process steps and new design as well as trouble shooting I have done.

All the process except the electron beam lithography are done in WCAM (Wisconsin Center for Applied Microelectronics). In Fig.3-1, the layouts of the HallDot chip and schematic diagram of the process steps are shown. As it can be seen, I first define Hall bars, and then integrate gate metals around the Hall bar in order to form a quantum dot in the middle of the Hall bar. The figure does not include the final step, which is electron beam lithography in the middle of the Hall bar where the gates (yellow outlines in step 3, top view) are converged together. I will discuss the electron beam lithography later. First, Hall bar patterns are defined by mesa etching, using SF6. The

S1813 positive Photo resist (PR) was used as the etch mask. Etch depth target depends on the depth of the 2DEG. Usually our 2DEG is about 70nm below the surface, and etch depth is about 130~100nm to etch out the 2DEG outside the Hall bar region. Secondly, ohmic metal layers of Au(~10nm)/Sb(~5nm)/Au(~80nm) are deposited by thermal evaporation followed by 400˚C annealing with 30sec. The annealing temperature is set to be higher than the eutectic temperature for gold with silicon (363 °C), and that for gold with germanium (356 °C) [29]. When annealing, the surface between Si and Au will become liquid phase, and Sb can be easily diffuse into the material. This is the end of the Hall bar process. Usually, I only anneal one of the chips, and test it. If the ohmic contacts are successful and the Hall measurement shows a good result, I anneal rest of the chips, and try to deposit PR immediately after the annealing for the following gate metal process. The reason why I try to minimize the expose time of the chips to air after the annealing is because the ohmic contacts tend to degrade over time, if they are exposed to air. The reason why the contacts are degraded is not fully understood. It could be attributed to the oxidation of gold related defects. The degradation of Gold/Antimony contact to Si/SiGe has been reported by S.F. Nelson *et al* [29]. After the Hallbar process is done and testing one of the chip, Palladium (Pd) gate fingers deposition is following. The thickness of Pd is about ~150nm. As seen in Figure 3.1 step 3, these gates (yellow outlines) have wide pad area for wire bonding, and come all the way down to the middle of the Hall bar, where nano gates are defined by electron beam lithography. Palladium has a high work function (5.22~5.6), which makes higher shottkey barrier.

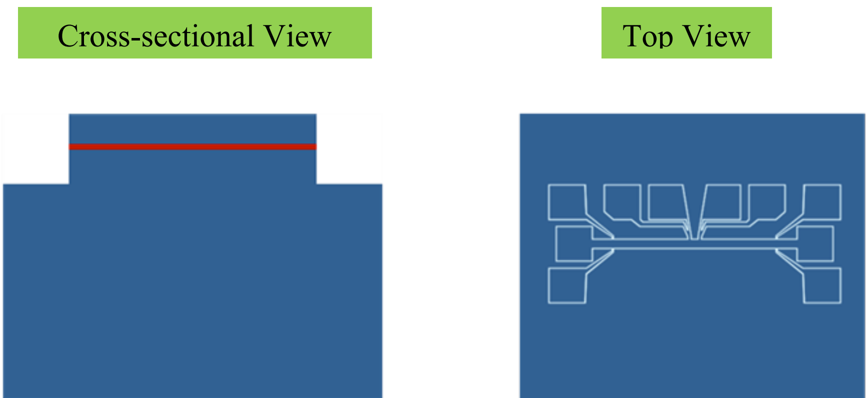

Step 1: Hall bar patterning, Plasma etching using SF6

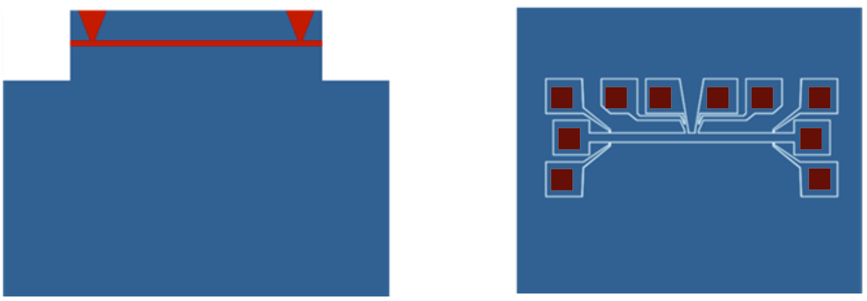

Step 2: Ohmic metallization, Au/Sb/Au deposition, annealing at 400˚C

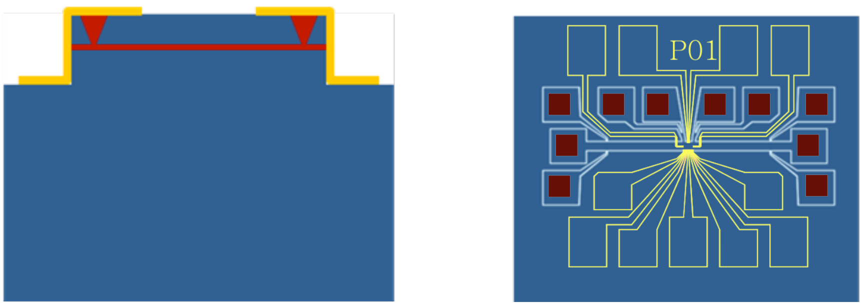

Step 3: Gate metallization, Pd deposition

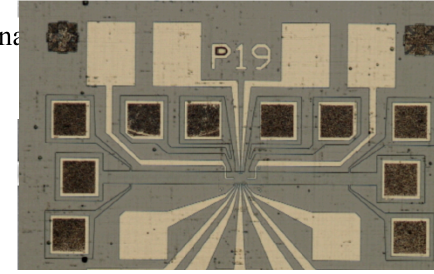

Figure 3.1: Fabrication flow of HallDot device. Left column: cross-sectiona
column: top view.

(a) (b)

Figure 3.2: Pictures of HallDot chip. (a) Optical micrograph of the whole chip. (b) Nano gates defined by electron beam lithography in the middle of the HallDot chip

The sample fabrication is almost done except the final and the core nano gates patterning by electron beam lithography. The principle of the electron beam lithography is much the same as optical lithography. Instead of UV light, electron beams are scanned on the resist. Instead of using masks for selective exposure, in electron beam lithography, the pre-loaded CAD structures are directly written on top of the resist. Therefore it is maskless lithography. Electron beam lithography is performed using LEO1530 SEM (Scanning Electron Microscope) at the Material science center. Regarding the resist, I used double layers of two PMMA (Poly methyl methacrylate) solutions with different molecular weights-150K and 500K. the 150K layer is coated first followed by 500K layer. When exposed, smaller molecular weight resist lead to slightly more area development, which create slight undercut underneath the above 500K layer. This undercut lead to successful lift off process. In Figure 3.2, a optical microscopy image of a completed Hall-

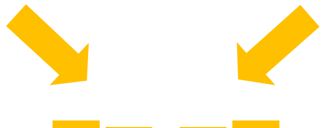

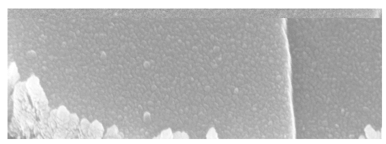

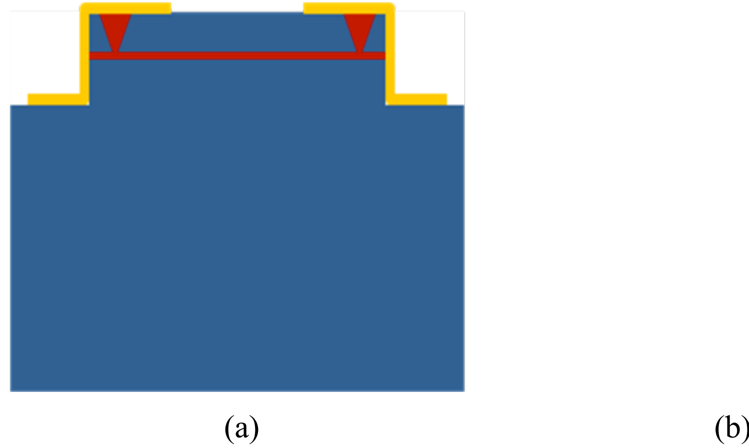

(a) (b)

Figiure 3.3: Angled deposition patching the break between optical gates and ebeam gates. (a) Schematic diagram of angled deposition. (b) SEM images of before (top) & after (bottom) angled deposition

Dot chip and a SEM image of one of the gate geometry used in the research are shown.

One of the troubles I had in sample fabrication was disconnection between gates defined by optical lithography (optical gates), and small gates defined by electron beam lithography (ebeam gates). This happened when there are lips around the edge of the optical gates. Following metal deposition after ebeam lithography would not be connected because the ebeam evaporation is very directional process that there are shadows around the lips as shown in Figure 3.3(b). To avoid this problem, I did additional electron beam lithography on those junction areas between ebam gates and

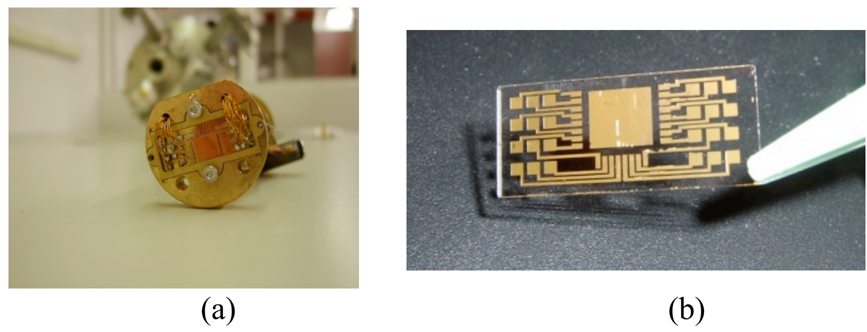

(a) (b)

Figure 3.4: Sapphire chip carrier. (a) Gold patterned sapphire chip. (b) Sapphire chip carrier mounted in the copper housing

optical gates, then did angled deposition, loading the sample 45degree tilted as shown in Figure 3-3(a). This will result in deposition of Pd at sidewalls. Figure 3.3 (b) SEM image before and after the angled deposition.

After the fabrication of the chip is complete, the chip is mounted on a sapphire chip carrier, on which gold pads are deposited for wire bonding and electrical connection to the tailpiece. Wire bonding needs to be done with care, since ebeam gates are sensitive to electrostatic discharge. To avoid a electrostatic damage, all the gates are tied together and shorted to the ground while wire bonding. The gates remain tied together until the sample is loaded in the insert, and connected to the measurement circuits because those actions to make electrical connection such as connecting cables to the insert may also causes a static damage. Fig.3-4 shows the pictures of the sapphire chip carrier and the copper housing that the sapphire chip carrier is mounted.

Sample screening was done before loading a chip in the dilution refrigerator. Sometimes samples fail at a cryogenic temperature mainly due to ohmic contact failure-contacts are frozen-causing open circuit. It is very frustrating to find out the sample failure after cooling it to the base temperature, which takes one of two days with many procedures. Warming up the fridge, replacing the sample, and cooling back again takes a lot of efforts and time. Therefore, pre-screening of those samples that could potentially fail help a lot increase through put of sample measurement. I screened the sample at 4K by putting it directly into the liquid helium Dewar using the vacuum insert with DC lines, which is called "dunker stick". This only takes a few hours to check the sample, and the procedure is much easier than dilution refrigerator. Once the sample passes the 4K screening, it is good to put it to the dilution refrigerator as soon as possible to avoid possible sample degradation.

3.3 Low temperature set-up

In this research, I used a commercial ^{3}He/^{4}He4 dilution refrigerator-Oxford's kelvinox MX4400 with a base temperature of 26mK. The principle of the operation is following. When a mixture of ^{3}He and ^{4}He4 is cooled below approximately 870mK, the mixture undergoes spontaneous phase separation to form a ^{3}He-rich phase (the concentrated phase) and a ^{3}He-poor phase (the dilute phase) as shown in Figure 3.5. Since the enthalpy of the ^{3}He in the two phases is different, it requires energy for

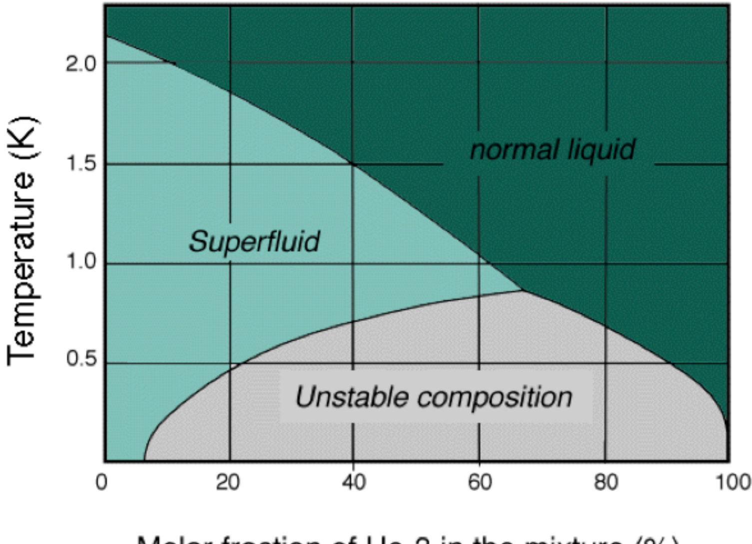

Figure 3.5: Phase diagram of ^{3}He – ^{4}He [30]

evaporation of ^{3}He from the concentrated phase into the dilute phase, which provide highly effective cooling. The principle is much like the same as how coffee cools. In a gross simplification, the concentrated phase of the mixture is pretty much liquid ^{3}He, and the dilute phase is effectively ^{3}He gas. The ^{4}He composing the bulk of the dilute phase is inert and non-interacting, and may be neglected. The evaporation of ^{3}He from the "liquid" phase to the "gas" phase cools the sample. This process works even at the lowest temperatures, because the equilibrium concentration of ^{3}He in the dilute phase is finite (about 6%, from the Figure 3.5) even at zero temperature.

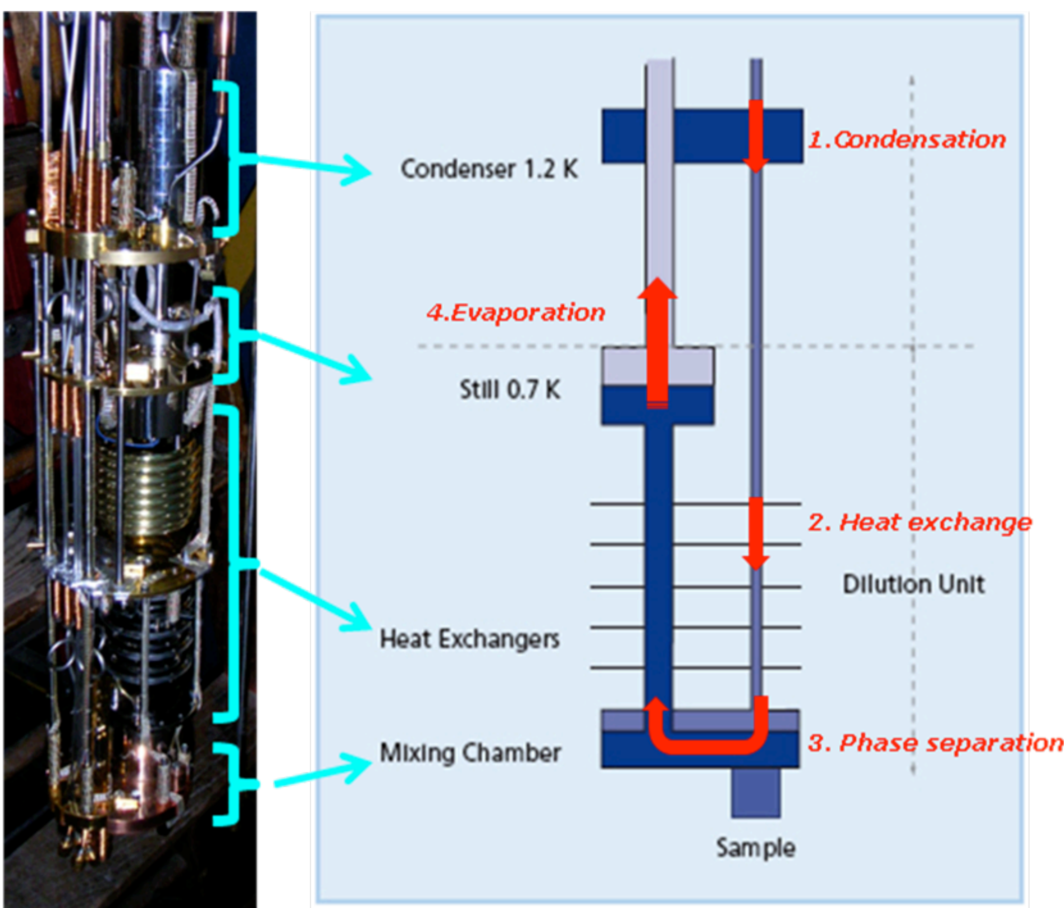

Figure 3.6: Dilution refrigerator and its schematic diagram showing flow of ^{3}He. Left: Photograph of the dilution unit. Different temperature stages are indicated by braces and matched with diagram on the right side. Right: Schematic diagram with flow of ^{3}He indicated with red arrows.

In Figure 3.6, the photograph of the dilution unit and the schematic diagram of the dilution refrigerator are shown. The closed cycle of ^{3}He flow is shown as a red arrow. Pumped from the still, the ^{3}He is brought back to 1K pot after filtered by liquid nitrogen and liquid helium filters. Being condensed in the 1K pot, ^{3}He is further cooled and pressurized when it pass through impedance lines and heat exchanger until it is got back to the mixing chamber. The ^{3}He is pumped again and the cycle continues.

Electrical Wiring is not a trivial job. Actually it is one of the most important factors not only to the signal quality, but also to cooling of a sample. Heat dissipation from a sample at below 0.5K is mostly done by electron diffusion through DC wires attached to the ohmic contacts, because cooling through substrate is very inefficient due to weak electron-phonon coupling at that temperature [31,32]. Therefore, below mixing chamber, high thermal conductivity wires such as copper or silver plated copper wires are used to maximize heat sink from the sample. In our fridge, diameter .010 CDA copper, insulated with Heavy Formvar (From California Fine Wire) wires are used. Above mixing chamber, low thermal conductivity wires are used to minimize thermal coupling to room temperature. To filter the noise, two filter stages are installed at the dilution unit. First, a RC low pass filter board is installed on the mixing chamber. Resistors are less noisy at low temperature. So it is better to install it at cold stage instead of at room temperature. The photograph of the filter board is shown in Figure 3.6(a). Twenty-four channels of RC filters are integrated in the PCB (Printed Circuit Board) to filter the low frequency noise in DC lines. Jon Prance from Mark Eriksson group designs the board in

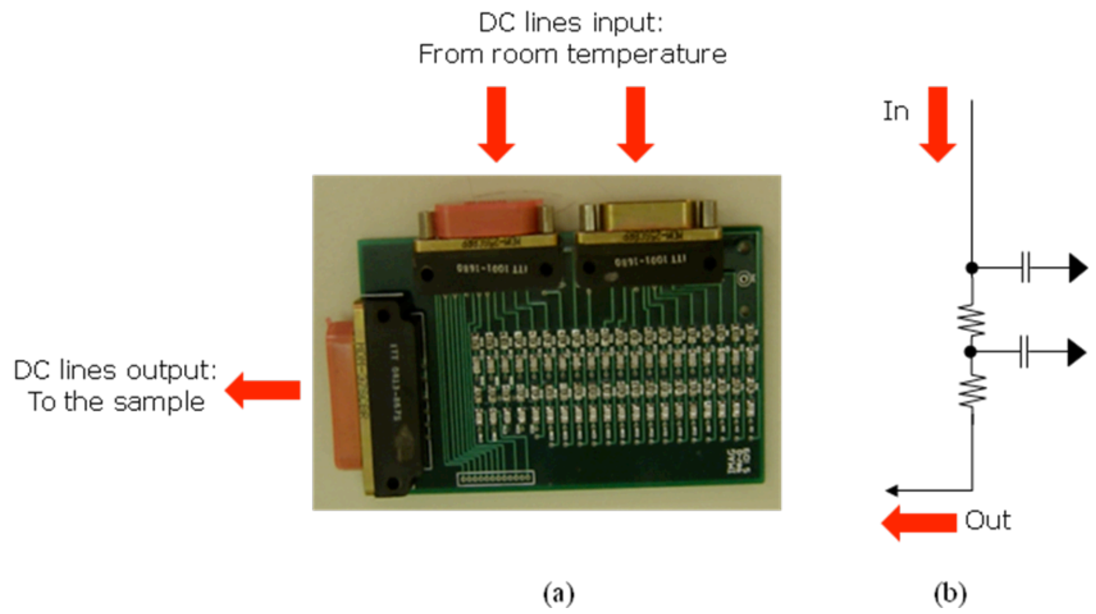

Figure 3.7: (a) A photograph of the PCB, RC low-pass filter banks with 24channels, installed at the mixing chamber. (b) The circuit diagram of one of the channels.

Physics department. Figure 3.6(b) shows circuit diagram of one of channel. Secondly, a cooper powder filter is attached at the bottom of the mixing chamber as a part of the tailpiece. It contains very small copper grains tightly packed in the gold plated copper housing together with the DC lines. A metal powder filter is used for two purposes. First, it serves as a heat sink, Secondly, and more importantly, it filters out high frequency noise. High frequency noise, propagating in DC wires with a form of evanescent wave is attenuated by nearby copper powder by skin effect [33,34].

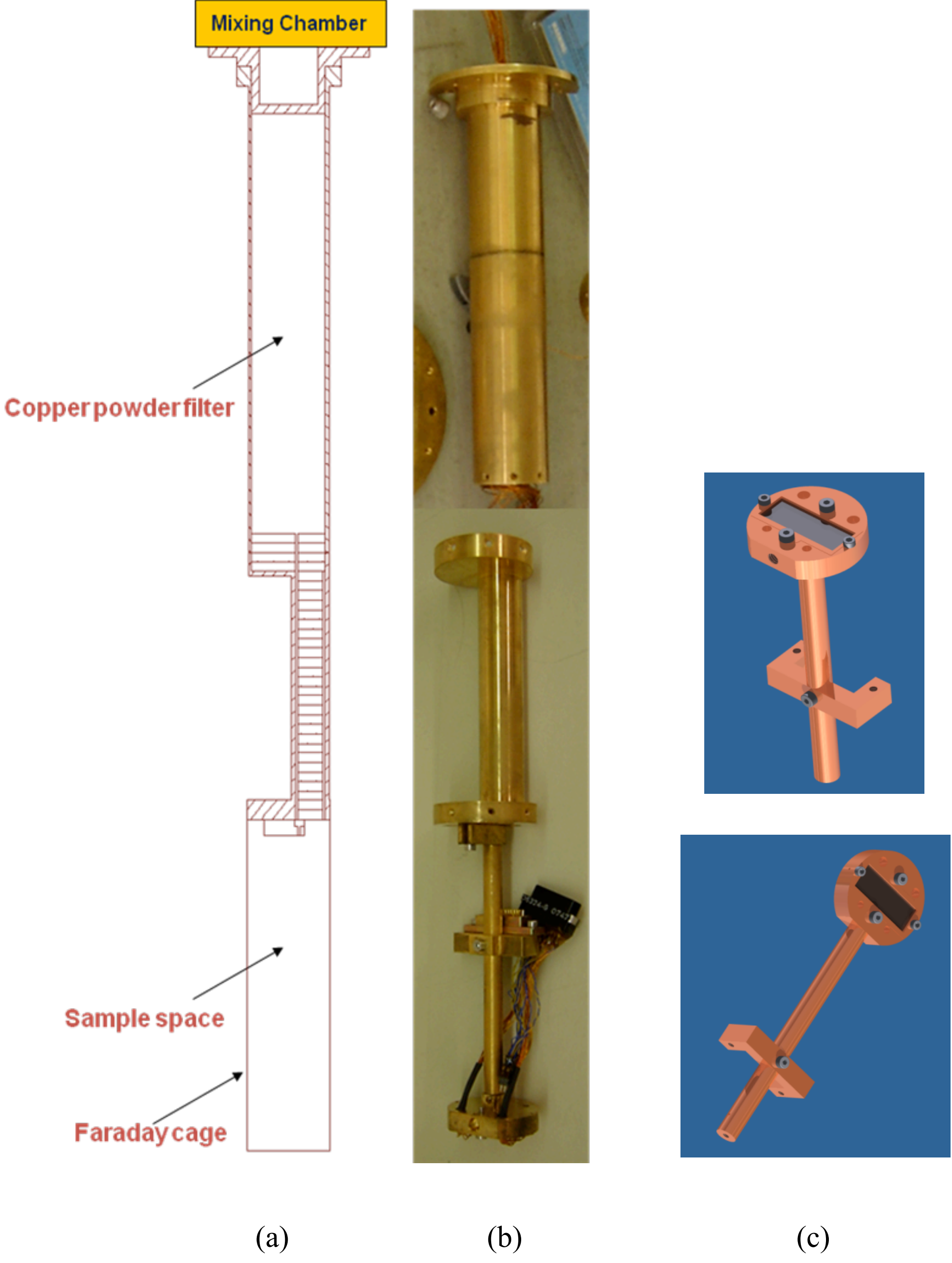

(a) (b) (c)

Figure 3.8: The tailpiece. (a) 2D CAD drawing with labels for each stage. (b) Photographs of the copper powder filter housing (top), and the sample holder with the sapphire chip carrier (bottom). (c) 3D CAD drawing of the sample holder with the chip carrier, showing two possible assembly schemes.

The smaller the grain size gives more filtering, since effective surface area that absorbing noise power is increased. Below the mixing chamber, copper powder filter and the sample holder is attached. These two stages are connected in series and called tailpiece. In Figure 3.7(a), the CAD drawing of the tailpiece is shown with labels for each stage. A faraday cage shields the sample space. In Figure 3.8(b), photographs of the sample holder and the copper powder filter housing are shown (The photograph of the copper powder filter was taken before completing the fabrication). In the photograph of the sample holder (bottom), the sapphire chip carrier is assembled in order to have the magnetic field perpendicular to the sample. It can also be assembled to have a parallel magnetic field as shown in Figure 3.8(c), which are 3D drawings of the sample holder with two possible assembly schemes.

Chapter 4

Tunnel barrier in a top-gated Si/SiGe quantum device

4.1 Introduction

Quantum mechanical tunneling is one of the most popular example to contrast the difference between classical and quantum mechanical behavior of electrons. Throughout history, it has been used to explain a range of physical phenomena such as the ionization of atomic hydrogen [35] and nuclear decay of alpha particles [36]. In semiconductor, Leo Esaki first demonstrated resonant tunneling diode, where he noted negative differential resistance (NDR) in 1958 [37].

In this chapter, I will talk about the tunneling experiment on a top-gated Si/SiGe quantum device. In section 4.2, I will talk about experimental detail, including electrical properties of 2DEG, measurement circuit and device structure. Then I will show tunneling conductance data. Modeling works based on 2D enclosed geometries are introduced in section 4.3. Finally I will discuss about the comparison of 2D modeling results with conventional 1D rectangular barrier model in section 4.4.

4.2 Experiments

Tunneling experiments were performed on a top gated Si/SiGe dot device. The purpose is to experimentally study barrier information such as height of shape of the barrier, and to use the experimental conductance data in barrier modeling, which is discussed in 4.3. We measured differential conductance on a tunnel barrier formed by one pair of top gates as functions of gate voltage, V_g, temperature, and drain-source bias voltage, V_{ds}. A scanning electron micrograph of the device is shown in Figure 4.3. The gate geometry in this device allows forming a single dot in the middle with two quantum point contacts for charge sensing [42]. Away from the dot area, there are gate pairs that can be used to form quantum point contacts with 45 degree tilted with respect to the crystallographic direction. Originally, this gate geometry was designed to study effect of atomic steps in valley splitting by quantum point contact energy spectroscopy. However, in this experiment, we only used one of the 45 degree tilted gat pair to form a single, gate controlled tunnel barrier. The specific gate pair used in the experiment is similar to the one shown in Figure 4.3(b).

The Si/SiGe heterostructure ID used in the experiment is '11012801.' It is grown on n-type silicon, and it has 2 degree miscut toward [010] direction. The two-dimensional electron gas (2DEG) is located approximately 75 nm below the surface of the Si/SiGe heterostructure. The carrier density and mobility of the 2DEG determined from Shubnikov-de Haas oscillations are $3.94 \times 10^{11}cm^{-2}$ and $102000cm^2V^{-1}S^{-1}$ respectively.

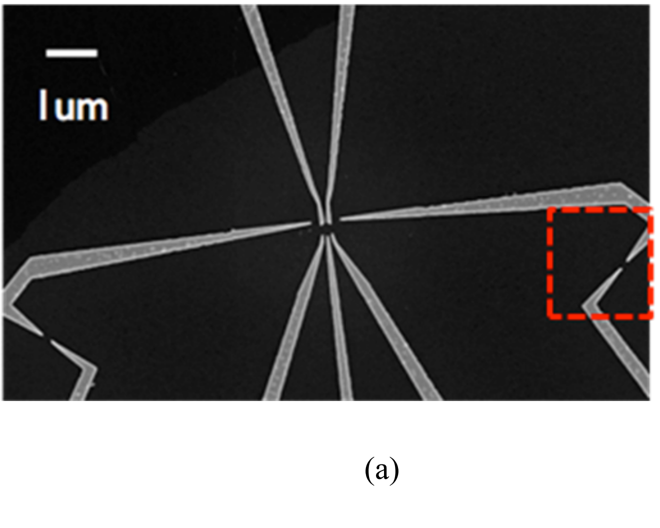

(a)

(b)

Figure 4.1: A scanning electron microscope images of the gate geometry identical to the one used in the experiments. (a) Gate geometry. (b) Zoom-in image of the gate pair used to form the potential barrier used in tunneling experiment.

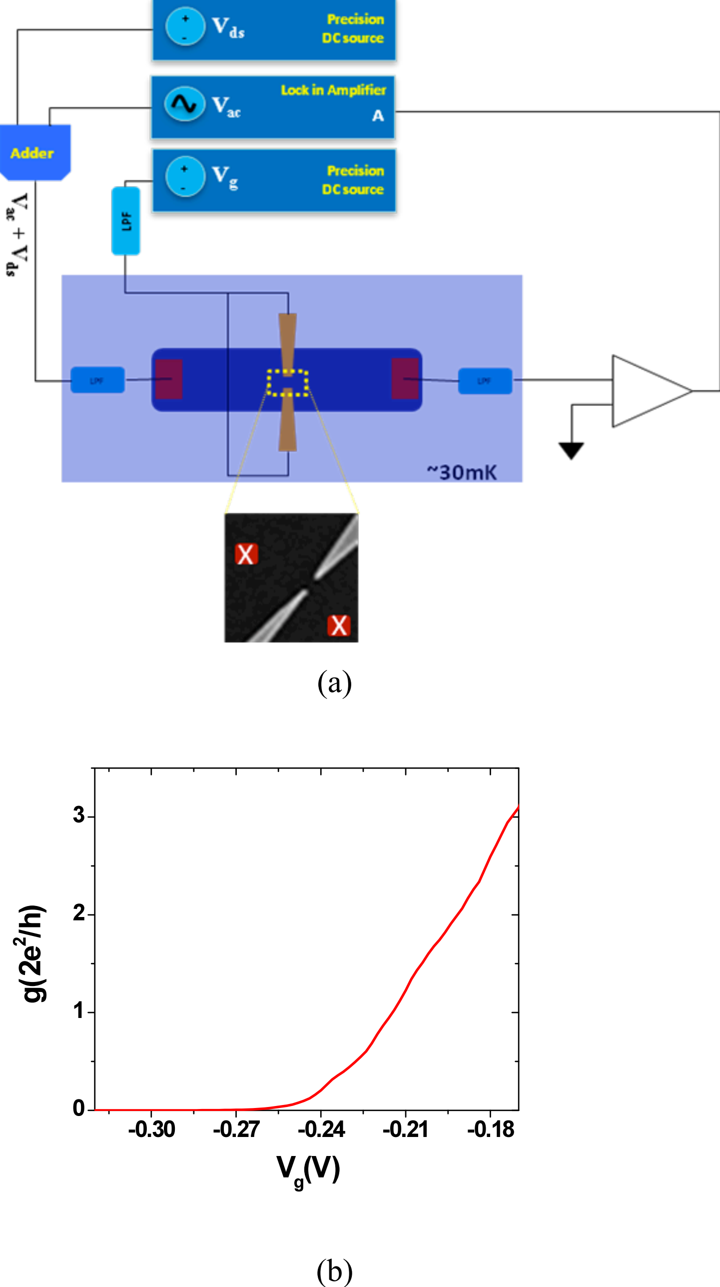

(b)

Figure 4.2: Measurement circuit and the pinch off characteristic of the top gate pair: (a) Schematic diagram of the circuit used in differential conductance measurement. (b) The pinch off characteristic of the differential conductance of the gate pair used in the tunneling experiment.

The device was measured in the dilution refrigerator with a base temperature of 30mK. Low frequency lock-in technique was used to measure differential conductance using ~10μV_{rms} AC signal, V_{ac}, on top of a DC bias, V_{ds}, across the source and drain. In Figure 4.2(a), schematic diagram of the circuit is shown. The reference source from the lock-in amplifier (Advanced Measurement Technology Inc., Model 7265) was used for V_{ac} and the DC bias is supplied from a precision DC source (Yokogawa, Model 7651). A RC low pass filter with the cut off frequency of 5Hz is attached in front of the DC source to reduce the noise from the equipment. The AC signal is added to the DC bias using an analog adder. The AC current through the tunnel barrier is amplified in the preamplifier (DL instrument, Model 1211) and converted to a AC voltage signal. The AC voltage signal is then measured in the lock-in amplifier.

The pinch off characteristic of the channel between gate pair is plotted in Figure 4.2(b). It shows smooth pinch off, which indicates that there are no disordered dots between the gates. When the DC bias is very small, the device is in linear regime, where the tunneling conductance does not change with drain source bias. When the bias is large, the tunneling conductance becomes nonlinear, due to the distortion of the barrier as well as energy dependent tunneling. We found that the tunneling conductance remain linear when V_{ds}< ~100μV. We are interested in the linear regime, because we want to study the pure barrier information without distorting it. Also, the theory work that we are going to use in modeling work is valid in linear regime [15]. Temperature dependence of the linear conductance through the

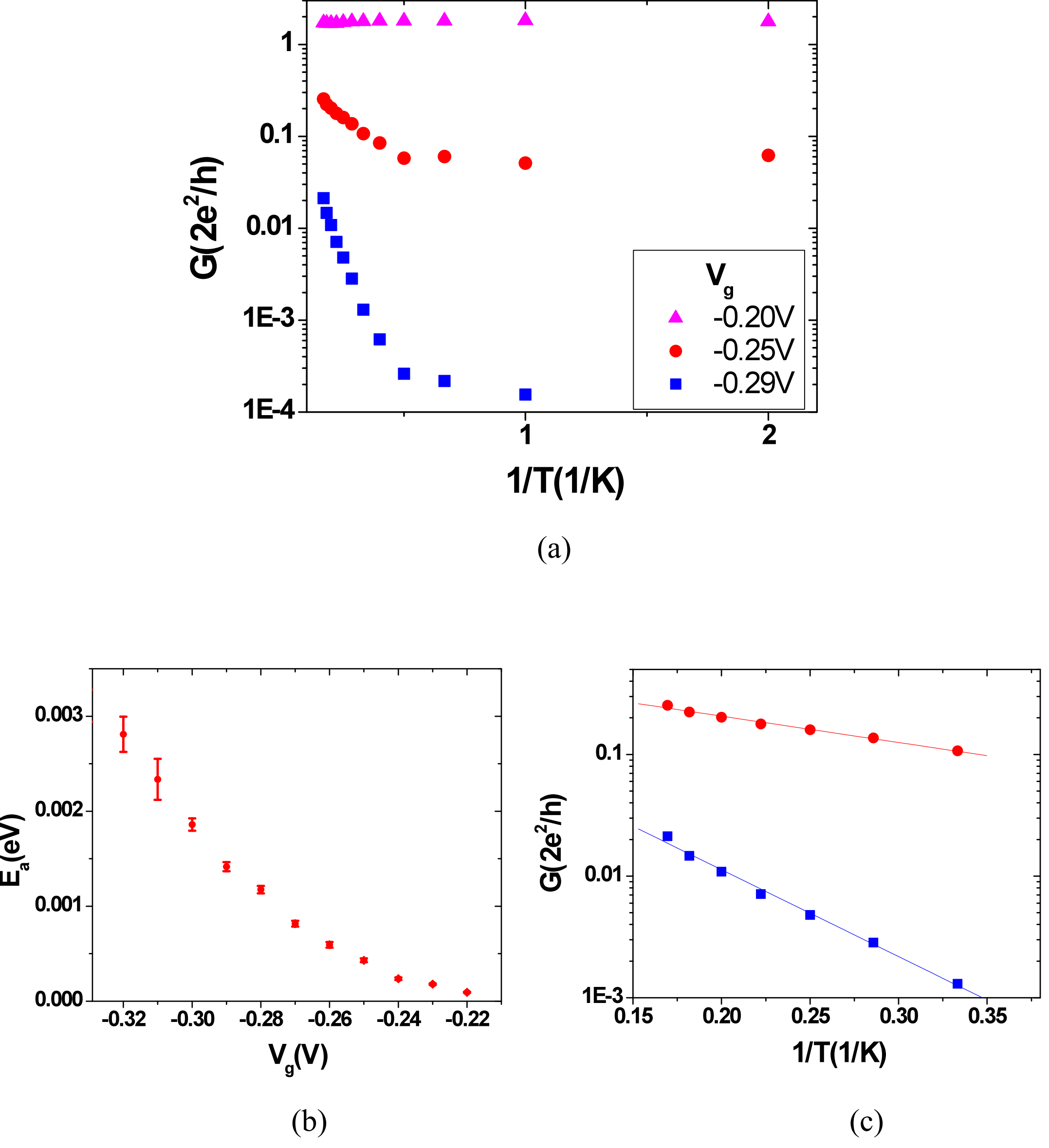

Figure 4.3: Temperature dependence of the tunneling conductance and activation energy. (a) Differential conductance through the potential barrier. Three exemplary gate voltages (color codes) are plotted against inversion of mixing chamber temperature (logarithm scale). (b) Activation energies determined from Arrhenius plot. (c) The data taken from (a) for V_g = -0.29V (blue dots) and V_g = -0.25V (Red dots) above 3K, and linear fitting to Arrhenius equation to determine the activation energy, E_a in (b).

barrier is useful to determine the height of the barrier. When the thermal energy is higher than the barrier height, $k_B T > eV_0$, where k_B is the Boltzmann constant, electrons acquire enough energy to overcome the potential barrier. As a consequence, conductance increases as temperature increases because more and more electrons can transport "over" the barrier instead of "tunneling" the potential barrier. Linear differential conductance as a function of Mixing chamber temperature and gate voltage is measured. The mixing chamber temperature range was from ~30mK to ~6K and the gate voltage range was, -0.33V < V_g < -0.18V. The data in Figure 4.3(a) shows three exemplary different gate voltages result. When V_g = -0.2V, temperature dependence is hardly seen. This is because the gate voltage is not sufficiently negative enough to form a potential barrier that is higher than Fermi energy yet, so the transport is not in the quantum mechanical tunneling regime. When V_g < -0.25V, the negative gate voltage becomes sufficient to form a potential barrier higher than Fermi energy. As shown in Figure 4.3(a), when V_g< -0.25V, there is strong temperature dependence in the conductance, as the temperature starts exceeding 1K. From this data, activation energy of the tunnel barrier can be determined by Arrhenius equation. Arrhenius equation is a simple, but remarkably accurate formula for the temperature dependence of a chemical reaction [43]. Using Arrhenius equation, the conductance as a function of the temperature can be written as

$$G(T) = A\exp(-E_a / k_B T) \tag{4-1}$$

where, E_a is the activation energy. Since Figure 4.3(a) is logarithm plot of the conductance against inversion of temperature, slope of the linear part of the data would give the activation energy by, slop = $-E_a/k_BT$. In Figure 4.3(b), activation energies for each gate voltages are determined plotted as a function of gate voltages. For this determination, we only made use of the temperature dependence of the conductance data above 3K, where the activation becomes clearly visible. The activation energy is exponentially increased as gate voltage become more negative. This implies that the barrier becomes exponentially taller and thicker as the gate voltages become more negative. Two examples of the Arrhenius plot fitting result at V_g = -0.25V, and V_g = -0.29V is shown in Figure 4.3(c).

The activation energy can be thought as a height of the barrier, $V_0 = E_a/e$, where V_0 is a height of a tunnel barrier. The reason is that at this energy or higher, the electron becomes just energetic enough to overcome the barrier. The activation energy has nothing to do with the length of the barrier, since the length or shape does not affect to the conductance much, when an electron has higher energy that the barrier height. This is very convenient fact for our barrier modeling work, because we want to develop models with only one input variable, gate voltage, and we can directly determine the relationship between a gate voltage and a height of the barrier from the activation energy data as a function of gate voltage shown in Figure 4.2(b). In the following section, we developed simple 2D barrier models. As introduced in Chapter 1, the motivation is to develop more

realistic model, treating the barrier as 2D, as well as to deduce the useful barrier information such as effective height and width, and energy dependent tunneling $|t^2|$.

4.3. Two-dimensional Modeling

The 2D barrier shape in a real device will be looking similar to the top gate structure of the device. To model such 2D barrier, one might think that it will be better to model the barrier as it is actually looking like. However, it will increase the complexity by creating too many parameters in a model. In reality, we only have one input parameter, the gate voltage. If there are too many parameters, all of which are functions of the gate voltage, it is too complex to parameterize them. Also, we are only interested in the information that affect to the tunneling conductance such as length and height. Therefore, it will be better approach to simplify the 2D barrier structure, to minimize the number of parameters, which are well defined by gate voltage. Simply speaking, as long as we can extract the interesting information, the simpler model is the better model.

Here, we developed simple 2D models with only two parameters each. We calculate the transmission coefficient, $|t^2|$ and the tunneling conductance, G from the

models, and fit the results to our experimental conductance data to make connection with real device.

The theoretical background for the modeling is developed in Ref. [15]. In the theory, single electron tunneling is considered in a closed 2D geometry with a symmetric barrier. Following to the theory, we consider simple but realistic 2D geometries describing the barrier formed by top gate. We solve 2D Schrödinger equation in the 2D enclosed boundary looking for solutions of symmetric and anti-symmetric eigenstates. The transmission coefficient is calculated using these egien energy by the equation:

$$|t_\alpha|^2 \cong \sin^2[(k_A - k_S)L] \tag{4-2}$$

$$= \sin^2 \left[\sqrt{2m^* L^2 / \hbar^2} (\sqrt{E_{A,\alpha} - E_{0,\alpha}} - \sqrt{E_{S,\alpha} - E_{0,\alpha}}) \right]$$

where $E_{S,\alpha}$ is the energy of symmetric eigenstate and $E_{A,\alpha}$ is the energy of anti-symmetric solution. $E_{0,\alpha}$ is the minimum energy of subband α, corresponding to the state with zero longitudinal momentum. $2L$ is the length of the 2D channel. For transport calculations, it is convenient to consider perfect leads, which are defined as regions where $\partial V / \partial x = 0$, so that k_x is a good quantum number. k_S and k_A are longitudinal momentum of the symmetric and anti-symmetric wavefunctions respectably. The Landaue-Buttiker formula for linear conductance is then given by,

$$G = \frac{e^2}{h} \sum_{\alpha} g_{\alpha} |t_{\alpha}|^2 \tag{4-3}$$

where g_α is the degeneracy of the system which is 4 in silicon case: 2 for spins, 2 for valleys. We focus only on the first subband. Based on our calculation, we found that the contribution of higher subbands to the conductance is negligible in the tunneling regime that we are interested in (we are interested in fairly opaque barrier regime where the total transmission probability is less than 0.1, which is consistent with physical dot system). We focus on the linear transport regime, where the relevant tunneling states are very near the Fermi level. We numerically solve 2D Schrödinger equations with effective mass approximation for transmission coefficient calculation using finite element method and equation (4-2). In the following, I divide the section into two, and talk about detail of the modeling. In 4.3.1, two models based on infinite barrier are introduced. In 4.3.2, two other models based on finite barrier are explained.

4.3.1. Infinite barrier models

Two models, based on infinite barriers are illustrated in Figure 4.4. For the convenience, we named the models. I will start with the first model in Figure 4.4(a),

which is called "Infinite Circular (IC) barrier model." The 2D barrier geometry is illustrated with dark yellow area. Yellow dashed line is the boundary of the 2D simulation cell. The length of the cell, l_c is 500nm long in x direction, and the width of the cell, w_c, is 60nm wide in y direction. The "perfect leads" can extend very far to the right or left in principle. However, the conductance is determined by the tunnel barrier, so the exact shape and length of the leads is not important.

We use only two parameters, width of the gap at $x = 0$, w_0 and the radius of curvature of the circular barrier, r as shown in Figure 4.4(a). They are all controlled by the only input parameter, gate voltage, V_g. By choosing this simple model, we are able to parameterize the model parameters in terms of V_g. We assume linear relations between V_g and the parameters. We fit the model to the experimental data and construct the parametric equations, $w_0(V_g)$ and $r(V_g)$.

Figure 4.4(b) is called "Infinite Rectangular (IR) barrier model." Similar to IC model, there are two parameters that control the tunneling conductance, the width of the gap at $x = 0$, w_0 and the length of the rectangular barrier, d. Likewise, We fit the model to the experimental data and construct the parametric equations, $w_0(V_g)$ and $d(V_g)$. The fitting procedure is explained with the flow chart shown in Figure 4.5.

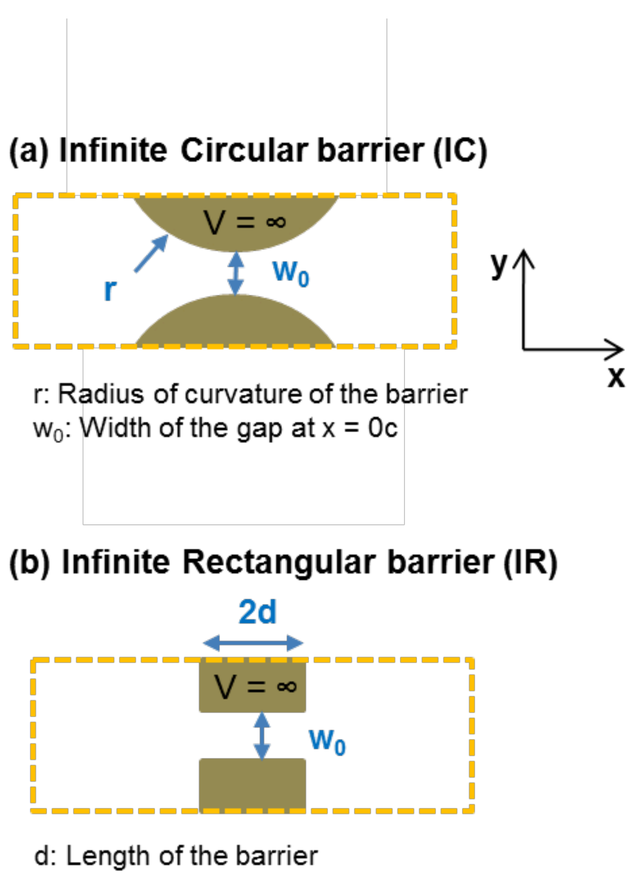

Figure 4.4: Illustration of the two infinite 2D barrier models developed in the work. (a) Infinite Circular (IC) model with the width of the gap at $x = 0$, w_0 and the radius of curvature of the circular barrier, r as parameters. (b) Infinite Rectangular (IR) model with w_0 and the length of the rectangular barrier, d as parameters. Tunneling direction is in x. Yellow dashed line indicates the boundary of 2D calculation that has width of 60nm and length of ~400nm.

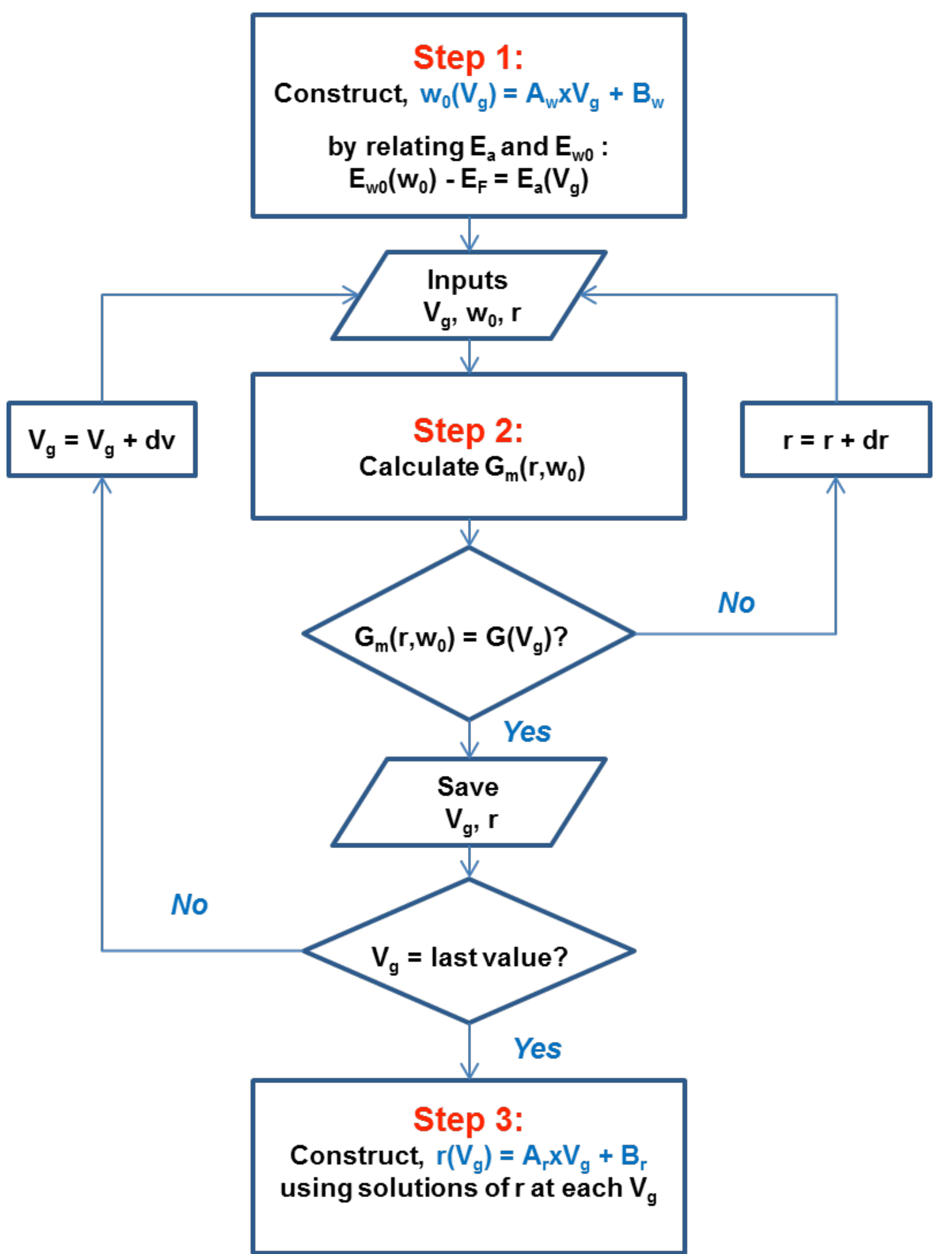

Figure 4.5: Flow chart of parameterization procedure for IC model

The first step is to determine $w_0(V_g)$ using the activation energy data. We somehow have to relate the gap size to a relevant energy scale. We do this by producing a 1D quantum well generated by cutting the 2D barrier along with *y* axis at *x* = 0. The "cross-sectional 1D quantum well" will have infinite barriers with the width of w_0. We assume that the first bound state energy of this quantum well, E_{w0} is the effective potential height at x = 0, because it is the lowest confinement energy when we put an electron at that position. The relationship between activation energy and E_{w0} is then given by,

$$E_a = E_{w0} - E_F, \qquad E_{w0} = \frac{\hbar^2 \pi^2}{2m^* {w_0}^2} \tag{4-4}$$

where m* is the effective mass. Equation (4-4) is a function of w_0. Therefore, we can relate $E_{w0}(w_0)$. and $E_a(V_g)$ to relate w_0 and V_g. In Figure 4.6, calculated $E_{w0}(w_0)$ and E_a (V_g) are plotted. By adjusting w_0, we were able to match two plots and extract the linear relationship between w_0 and V_g. The linear function, $w_0(V_g) = 4.88756e^{-8}+9.19836e^{-8}*V_g$.

In Step 2, we determine $r(V_g)$. At a given V_g, now we can fix w_0 using $w_0(V_g)$ found from step1, and work only with second parameter, *r* to fit the calculated model conductance as a function of w_0 and *r*, $G_m(w_0,r)$ to the experimental conductance, $g(V_g)$,

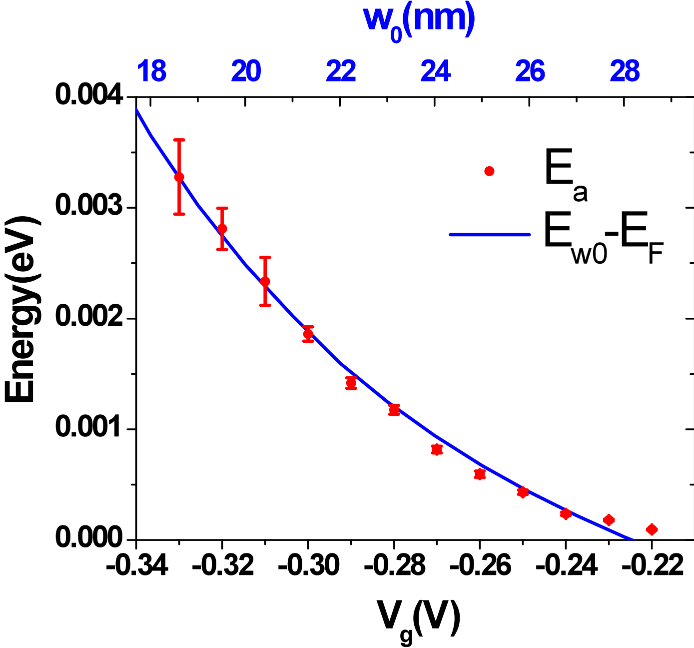

Figure 4.6: Fitting result of E_{w0} to E_a. Blue curve is E_{w0} as a function of w_0. Red dots are activation energy data from Figure 4.3(b), which is a function of V_g. By fitting these two results, linear relationship between w_0 and V_g is found.

which is shown in Figure 4.7(a). Then we calculate $G_m(w_0, r)$ as a function of *r* to find the solution at each V_g. We calculate this numerically using the commercial software, COMSOL v3.5a. The solutions of *r* at each V_g, and linear fitting are shown in Figure 4.7(b). Red dots are the *r*s and the blue line is the linear fitting with respect to V_g. We fitted the data with $V_g > -0.28$V, because it fits well only above that voltage. This is due to the kink around $V_g \sim -0.28$V in the experimental data in Figure 4.7(a). The reason why

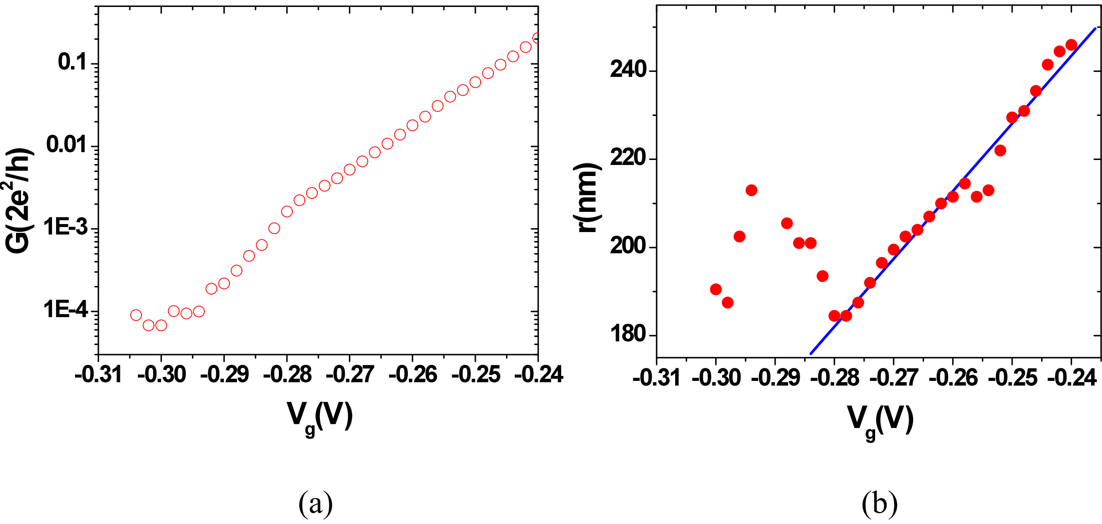

(a) (b)

Figure 4.7: Conductance data used for fitting r_i and fitting result. (a) Conductance data as a function of V_g, $G(V_g)$ (b) *r* values (red dots) that fit calculated conductance to the data shown in (a). Blue line is linear fitting of *r* with respect to the V_g.

the kink causes dramatic change in *r* is because the impact of *r* to the conductance is not big. The r has to change very much to reflect the sudden kink. The positive slope of the linear fitting is counter intuitive. We expect a negative slope, because applying more negative V_g should make the barrier wider and taller, therefore the r has to increase. The reason for it is that w_0 is much stronger impact on the conductance than *r*. As Vg goes to more negative value, w0 gets smaller, which causes reduction of the conductance so much that the *r* needed to decrease to fit the data. Although the trend is contradicting to the physics, it is OK since the model does not necessarily follow exactly what is

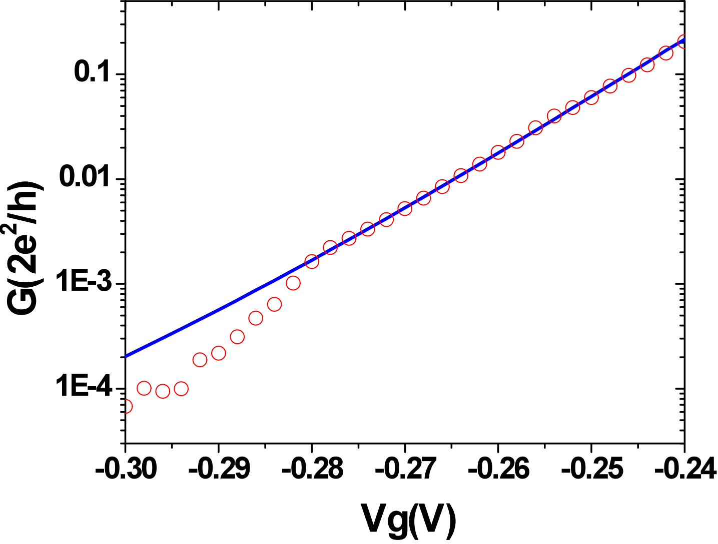

Figure 4.8: Conductance fitting result for IC model. Red dots show experimental data, $G(V_g)$ and blue line shows calculated conductance using two parametric equations, $G_m(Vg)$

happening in reality. What is important is that we have controllable parameter to model the experimental conductance, and we will discuss meaningful values that we extract from the models later. In step 3, we construct the parametric equation, $r(V_g) = 6.1241e^{-7} + 1.5370e^{-6} * V_g$. We finished the fitting process, and constructed two parametric equations, $w_0(Vg)$ and $_r(Vg)$, with which we can calculate the model conductance as a function of

V_g. We plotted the model conductance, $G_m(Vg)$ and the experimental data in Figure 4.8. The simulation agree well with the experimental data above V_g > -0.28V, since we only fit them in that range.

For IR model, similar fitting procedure was performed using the same algorithm shown in the Figure 4.5 . The result is summarized in Figure 4.9. (a) shows fitting result of d to V_g, (b) shows conductance fitting result. In IR model, the simulation fits entire range of V_g. This is because the linear fitting of d works much better than r. This means that w_0 is not dominant over d.

4.3.2. Finite barrier models

We also developed finite barrier models with similar geometries to IC, and IR. They are illustrated in Figure 4.10. For the convenience, we named the models. Figure 4.10(a) is called Finite Circular (FC) barrier model, and (b) is called Finite Rectangular (FR) model. Similar to infinite barrier models, there are also only two parameters for each model, the height of the barrier, V_0 for both of the models and the radius of curvature of the circular barrier, r for FC model, and the length of the rectangular barrier, d for FR model. The only difference between infinite model's geometry is that there is no gap, because we don't need it anymore having the finite height of the barrier in the

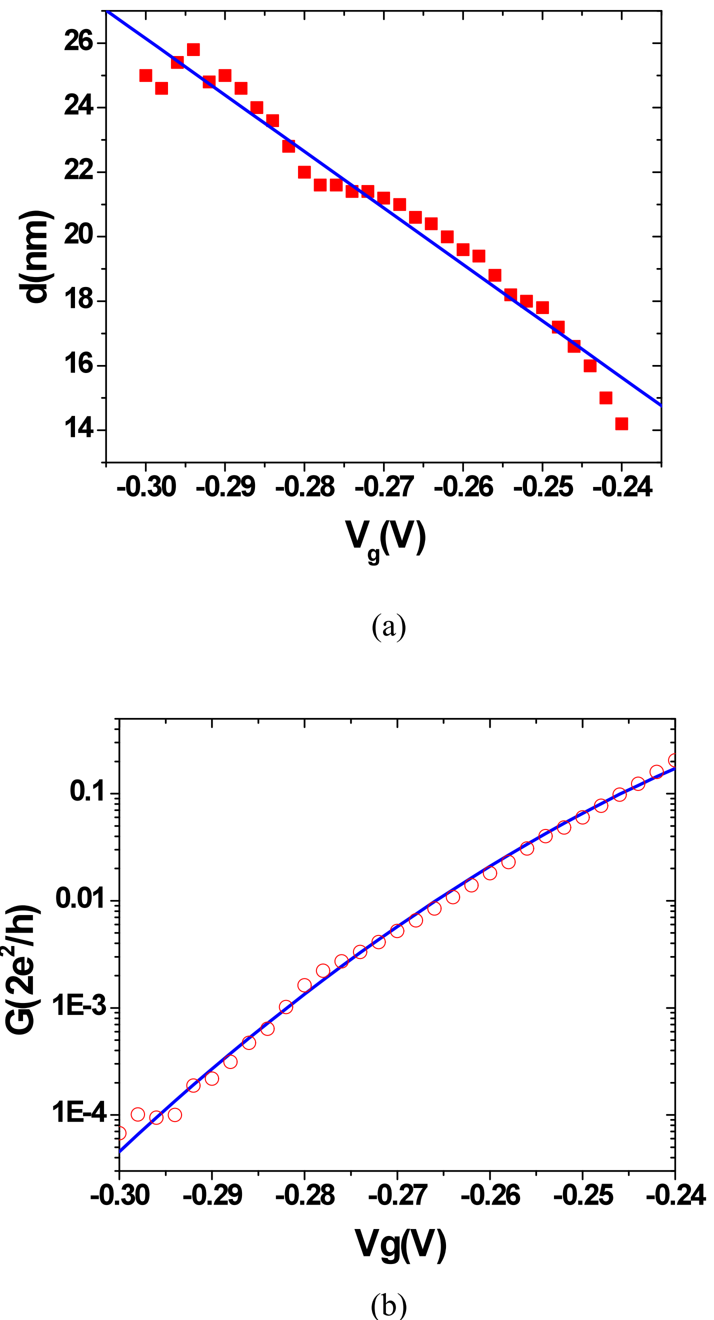

Figure 4.9: Fitting results for IR model. (a) *d* values (red dots) that fit calculated conductance to the data shown in (b). Blue line is linear fitting of l_i with respect to the V_g. (b) Conductance fitting result for IR model.

models. The parameterization procedure is basically the same as for infinite barrier models – finding relation between two parameters and V_g, so that the model conductance is only a function of V_g. As we did before in infinite barrier models, we first determine$V_0(V_g)$ using the activation energy. Since now we can directly assign the finite height of the barrier, we first fit the activation energy to into an exponential function of the gate voltage, and directly use it for $V_0(V_g)$. The fitting curve is shown with the data in Figure 4.11(a). The fitting exponential function is shown in Appendix D. To make the activation energy is equal to the height of the barrier in the model at *x* =0, we need to include the confinement energy in the lead. This is the minimum energy in the model, which is given from the finite width of the 2D simulation cell, w_c. All the energy in the model is measured from this confinement potential in the lead. Therefore, the total height of the barrier at *x* = 0, is equal to $V_0 + E_0$. We fit this energy to the measured activation energy by following equation

$$E_a = V_0 + E_0 - E_F, \qquad E_0 = \frac{\hbar^2 \pi^2}{2m^* {w_c}^2} \tag{4-5}$$

where, E_0 is the confinement energy of the lead. Using (4-5) we can determine $V_0(V_g)$. Next step is to determine $r(V_g)$ and $d(V_g)$, by fixing V_0 at each V_g. The procedure is same

as for IC and IR model respectably, so I would not explain here again. The fitting results for FC and FR model are summarized in Figure 4.11(a) to (d).

The FR model In Figure 4.11(b), the fitting results for *r* (top) and *d* (bottom) are shown. To the contrary with IC model, in FC model, the *r* increases as V_g goes to more negative regime, which is consistent with the physical picture. All parametric equations are listed in Appendix D.

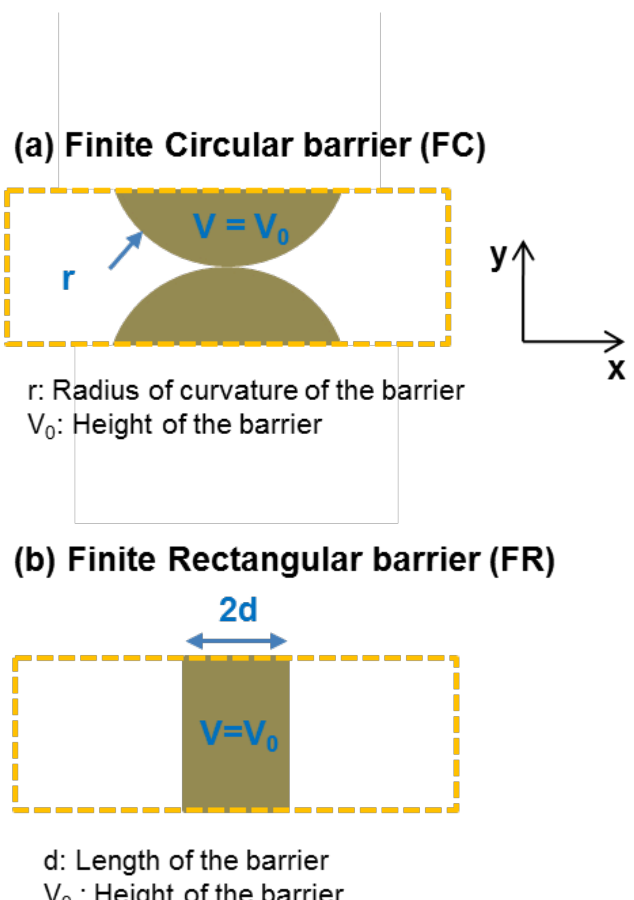

Figure 4.10: Illustration of the two Finite 2D barrier models developed in the work. (a) Finite Circular (FC) model with a finite V_0 and the radius of curvature of the circular barrier, *r* as parameters. (b) Finite Rectangular (FR) model with V_0 and the length of the rectangular barrier, *d* as parameters. Tunneling direction is in *x*. Yellow dashed line indicates the boundary of 2D calculation that has width of 60nm and length of ~400nm.

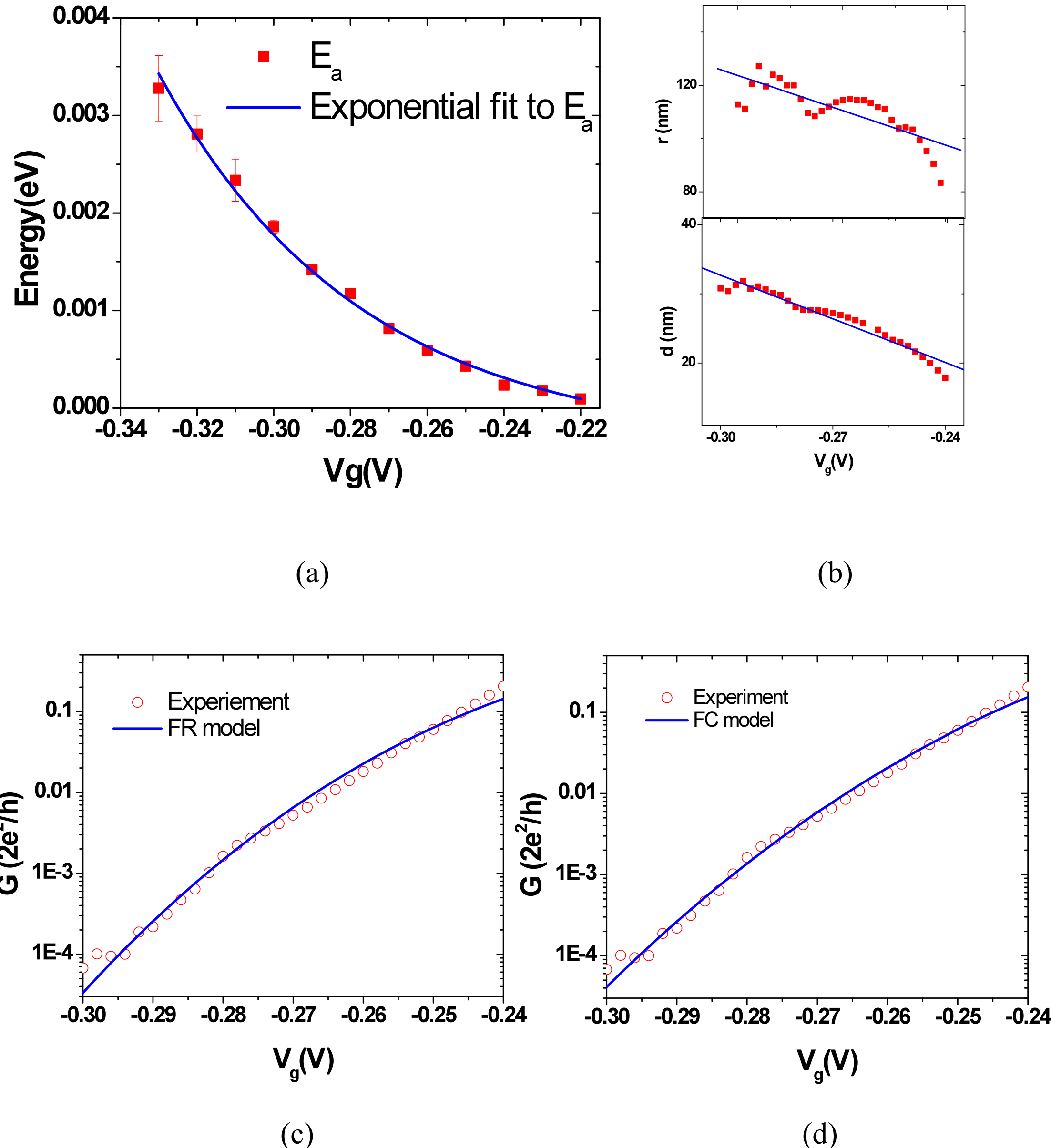

Figure 4.11: Summary of finite barrier modeling results. (a) Exponential fitting of E_a to construct $V_0(V_g)$. (b) Fitting results for r (top) and d (bottom) which are used to construct $r(V_g)$ and $d(V_g)$. (c) Conductance fitting of FR model (d) Conductance fitting of FC model. Red dots show experimental data and blue lines show model conductance, $G_m(V_g)$.

4.4. Effective 1D barriers

Up to now, we finished development of 2D models that fit to experimental conductance. Yet, we have not figured out what information we can deduce from the models and if they are useful. Also, we want to compare our 2D models result with the conventional semi-classical one dimensional (1D) square barrier model approximation, to validate our hypothesis that conventional 1D approximation is not proper to model this kind of barrier.

For that reason, we extracted an effective 1D barrier potential profile from each 2D models. The benefits of this dimensional conversion is that 1) it makes the comparison with 1D model easy by matching the dimensionality, 2)we can deduce the important information about our barrier shape such as 1D effective barrier height and length, which is critical to understand energy dependent tunneling. To extract an effective 1D barrier profile, we use the same approach that we used to determine the height of the barrier with cross-sectional 1D quantum well bound state energy. Since the width of the quantum well is a function of x, we can extract effective barrier heights, $V_b(x)$ as a function of x. The extracted 1D barrier is illustrated in Figure 4.12(a) to (d) for each model. In the circular barrier models, we expect parabolic shape because the width increases as moving away from x=0. For RC model, the cross-sectional 1D quantum wells have two steps of the potential height due to the background confinement from the

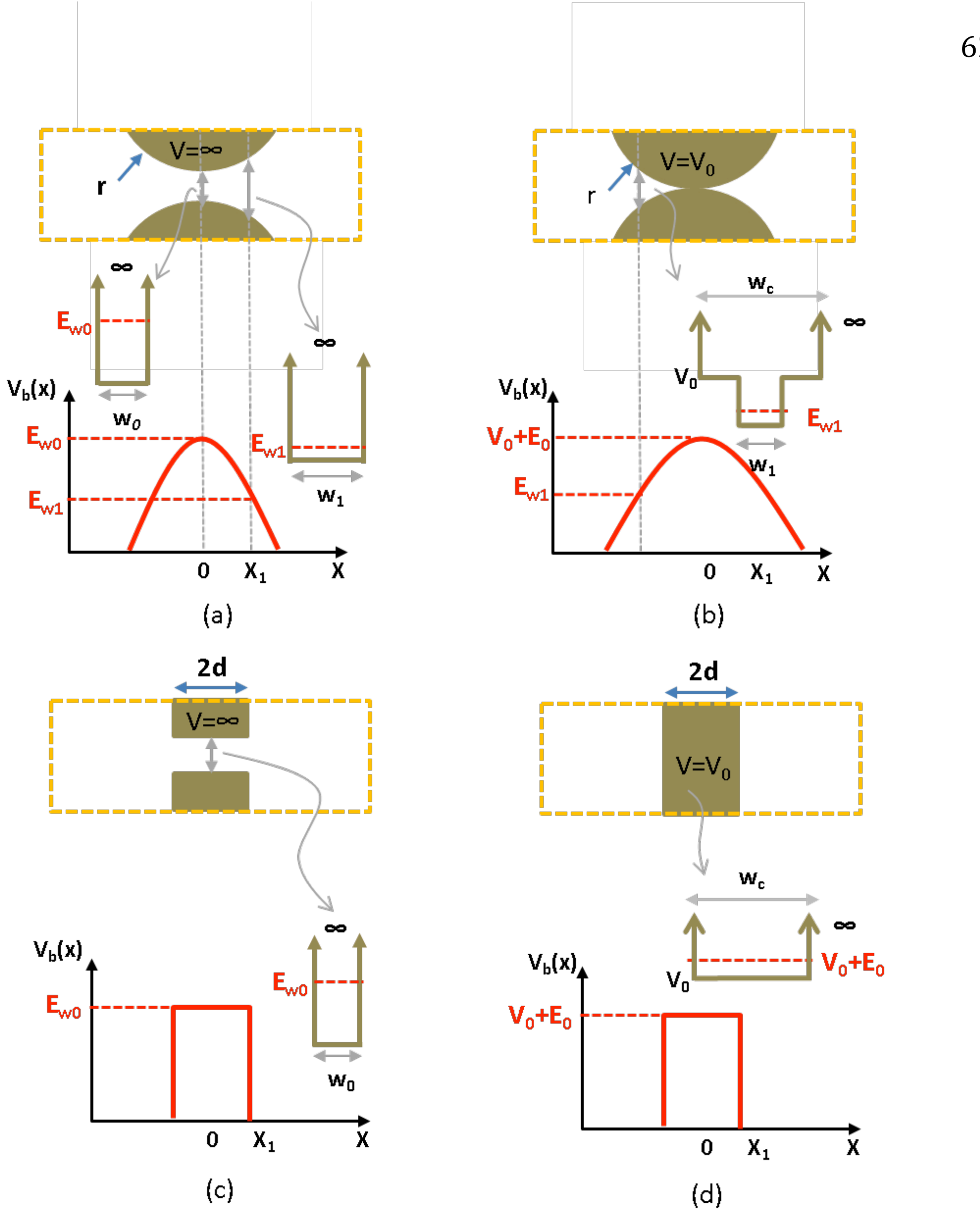

Figure 4.12: Illustrations of how to extract effective 1D barriers from the 2D models. Energies of the cross-sectional 1D quantum wells in y direction are used as approximated height of the barrier at given x. (a) IC model. (b) FC model. (c) IR model. (b) FR model.

calculation window as shown in Figure 4.12(b). For rectangular barrier models, it simply becomes 1D rectangular barrier width a barrier length decided by 2*d*. Figure 4.13 shows examples of the extracted 1D effective barrier profiles for each models. The specific gate voltages for all profiles are -0.3V. From the extracted 1D barrier, we determined the effective length of the barrier, L_b. For rectangular barrier models, it is the same as 2*d*. For circular barrier models, it is not easy to determine in a direct way. We approximate an effective length of the circular barrier it as the full width half maximum (FWHM) above the Fermi energy.

For 1D modeling, we use the simple 1D rectangular barrier based on WKB approximation, introduced in Appendix C. In this model, there are two parameters, height of the barrier, V_0 and length of the barrier, *a* to calculate the conductance. The tunneling conductance is given by equation (4-3), and we use (C-24) for calculation transmission coefficient. To be consistent with 2D models, we determined the height of the barrier as E_a. As we did for 2D models, we then fix V_0, and determined the length of the barrier for each V_g.

The length of the each models are plotted in Figure 4.14. There are some variations of L_b among 2D models. In general, finite barrier models always show longer barriers than infinite barrier models, mainly due to the differences in the type of the potential barrier. To compare IC and FC, at less negative voltage regime, two models

show similar effective length. In highly negative voltage regime, the gap between two model increases. This is because the gap size, w_0 is much stronger effect than *r* in IC model, that r has to decrease as w_0 decreases as explained earlier in 4.3.1.

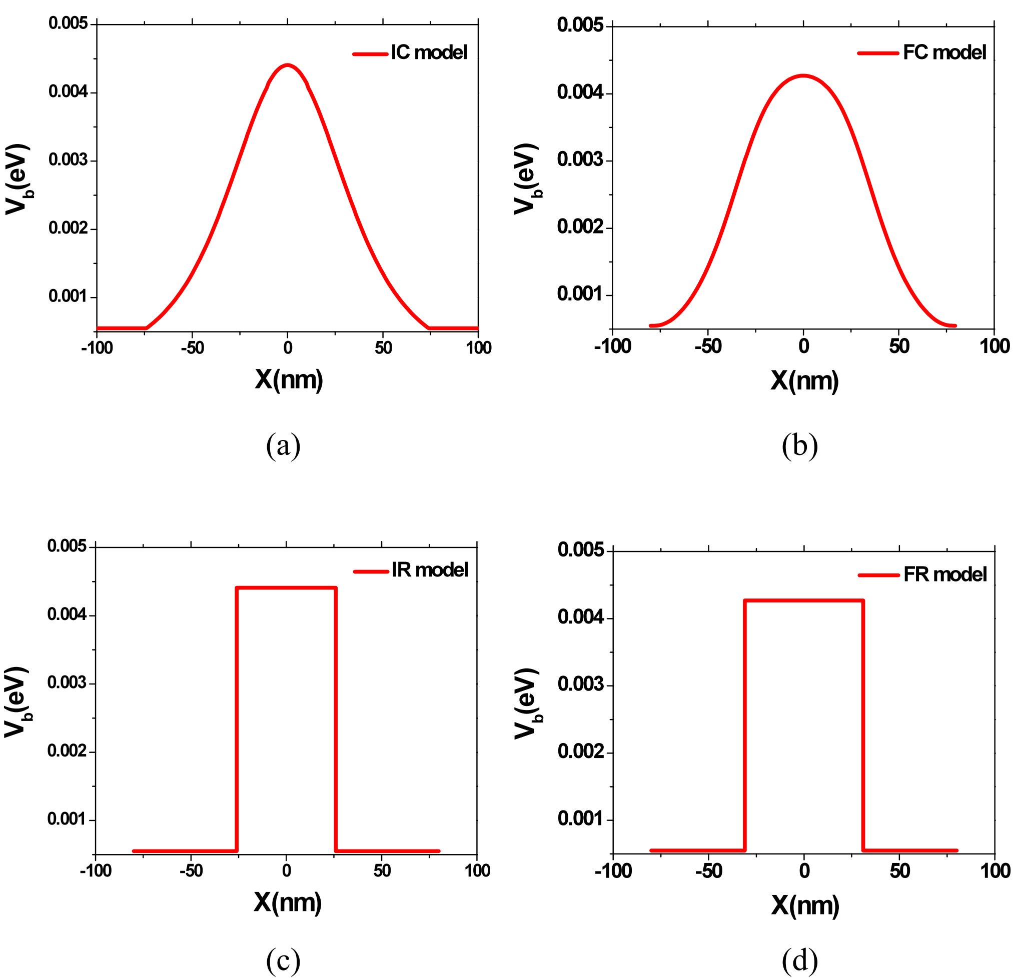

Figure 4.13: Effective 1D barriers extracted from the 2D models. (a) IC model. (b) FC model. (c) IR model. (b) FR model. Gate voltages for all models are -0.3V

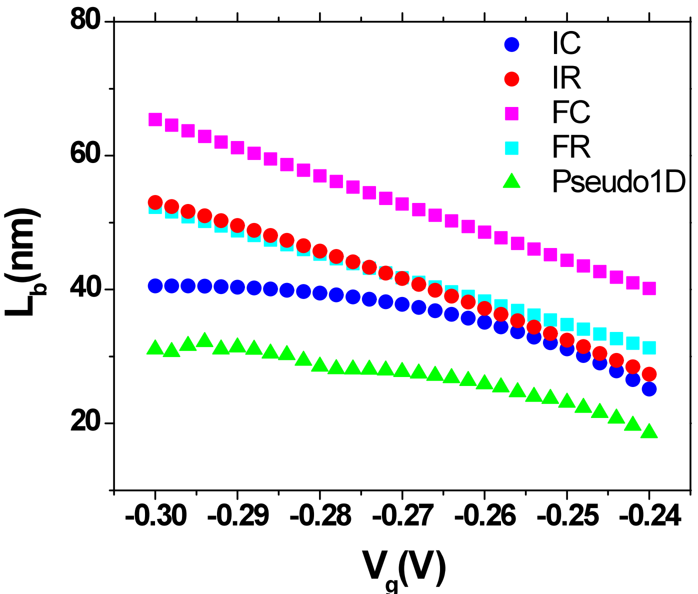

Figure 4.14: Comparison of effective 1D effective barrier length, L_b extracted from the 2D models and the length of the 1D rectangular barrier. Different Color codes are used for different models. All models show longer barrier length than conventional 1D model.

Chapter 5

Conclusions

5.1. Comparison of effective lengths of the barriers

We compared the effective lengths of the extracted 1D barrier among different 2D models and to 1D rectangular barrier length. Since we set the height of the barriers for all models as the activation energy, we can discuss the difference between models based on the length of the barriers. First of all, we want to emphasize that all 2D models result in longer effective lengths as shown in Figure 4.14. It certainly tells that consideration of the barrier as 2D, taking into account the wavefunctions in peripheral barrier region is necessary to describe this type of barrier. Second of all, we argue that the effective barrier lengths of the 2D models with $V_g < -0.28$ (~40nm to ~60nm) are reasonable value for a typical quantum dot using similar Si/SiGe heterostructure used in this experiment, where a Fermi wavelength is about ~56nm, and dot size is in the order or ~100nm. On the other hand, the 1D barrier length in the same V_g regime is about ~28nm to ~30nm, which is almost half of the 2D predictions. This supports the validity of 2D models over 1D

approximation. Lastly, all 2D models result in different effective barrier length, and the difference is consistent with the difference in the 2D geometry. This implies that geometric factors are preserved in 1D effective barrier, so that we can use the effective 1D information as genetic effect of the 2D barrier geometry.

5.2. Energy dependence of the tunneling conductance

We calculated the energy dependence of the tunneling conductance of the 2D models by plotting fractional change in tunneling conductance with respect to the conductance at Fermi energy, as a function of the differential of energy from E_F. The purpose of the calculation is to measure the level of the energy dependence of the conductance of the models, and compare it with experimentally determined energy dependent coefficient that are found from pulsed gate tunnel rate measurements from Ref.[11]. Energy dependent tunneling coefficient is defined as the exponential decay constatnt of the tunnel rate change in terms of energy,

$$\Gamma(E) = \Gamma_0 \exp(-E / E_i) \qquad (4\text{-}6)$$

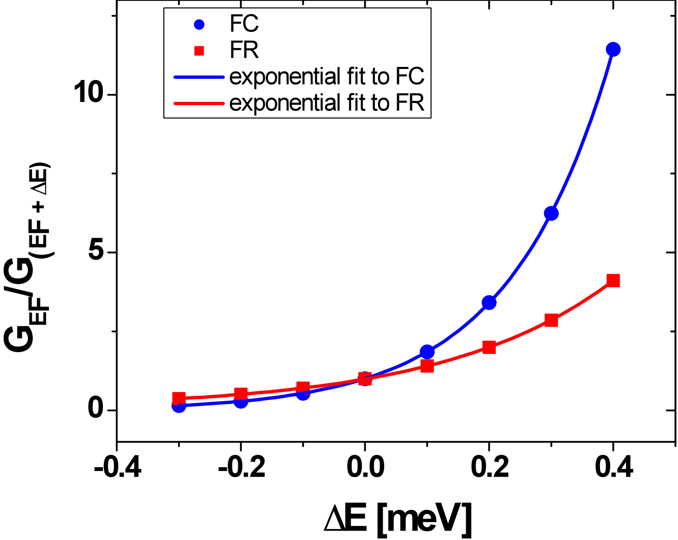

Figure 4.15: Fractional change of tunneling conductance as a function of energy. The fractional change calcualtion is referenced at E_F. Blue dots are calcuated using FC model and red dots are calculation from the FR model. For each data, we fit them into a exponential function to determine E_i

where, $\Gamma(E)$ is tunnel rate at a given energy, Γ_0 is initial rate and E_i is the energy dependent tunneling coefficient. In Ref.[11], E_is of different states in a Si/SiGe quantum dot are calculated based on pulsed gate tunnel rate measurement.

In our calculation, we determined E_i from fractional change of the tunnel conductance as a function of energy. Since tunnel rate is proportional to the tunnel conductance, it is possible to directly compare the calculated E_i to the experimentally determined values from Ref. [11]. In Figure 4.15, we plotted two examples of the energy

	1D	**IC**	**IR**	**FC**	**FR**
E_i(meV)	0.25	0.171	0.263	0.166	0.272

Table 4.1: Energy dependent coefficient,$E_{i,}$ for each model. All values are determined from the exponential fitting of the fractional change of the conductance plot similar to the plot in Figure 4.15.

dependence of the fractional change of the conductance as functions of differential of the energy. Then we fit the data into a exponential function to extract E_i. Calculated E_i from different models are listed in Table 4.1. Comparing to the experimentally determined E_i in [11], which are ~0.65meV to 0.195meV, we found that E_is from circulare gate models agree most well. We also note that the rectangular barrier models have higher E_i than circular barrier models due to the shape of the barrier. This implys that the barriers in real device is more like parabolic shape, instead of rectangular.

Appendix A

Electromagnetic field noise measurement in ME1166B

Abstract

Electromagnetic radiation (EMR) is the oscillation of electromagnetic field (EMF) that carries energy and information. EMR has both electric field and magnetic field components, which oscillate perpendicular to each other and to the direction of wave propagation. Strong electromagnetic field could reduce the performance of devices in the lab, influence the result of experiments and do harm to people's health. In this report the distribution and time dependence of EMF strength inside and outside the lab ME-B1166 are measured by a handheld EMF meter Extech 480836. From the distribution data, the dominate EMF sources are positioned. After that, the characteristics of the EMF distribution in the lab are analyzed. In the end, the data are fitted to different theoretical radiation models by MATLAB.

Introduction

Both of the **E** field and **H** field have three spatial components that can be measured independently by the EMF meter. Using the formulae below, the intensity of field can be obtained.

$$E = \sqrt{E_x^{\,2} + E_y^{\,2} + E_z^{\,2}} \tag{A-1}$$

$$H = \sqrt{H_x^{\,2} + H_y^{\,2} + H_z^{\,2}} \tag{A-2}$$

Then we can calculate power density (the rate of energy transfer per unit area), also known as the Poynting vector, indicating the power distribution of EMF in the space

$$S = \left|\vec{S}\right| = \left|\vec{E} \times \vec{H}\right| \tag{A-3}$$

For far-fields, where the distance to the field source is more than three wavelengths, EMF can be regarded as standard plane or Spherical wave where E is always perpendicular to H and proportional to H and the equation below holds true [38]

$$H = \sqrt{\frac{\varepsilon}{\mu}} E \tag{A-4}$$

Where ε is the dielectric constant and μ is the permeability. Then we got the expression of power density away from EMR source

$$\vec{S} = \vec{E} \cdot \vec{H} = \sqrt{\frac{\varepsilon}{\mu}} E^2 \tag{A-5}$$

(A-5) tells that **S** is only dependent on **E**, i.e. in the region away from EMR source, the distribution of EMF can be estimated by the distribution of **E** alone. Figure A.1 shows top view of the building structure around lab ME- B1166 (area inside yellow rectangle). The red spots indicate Wi-Fi antennas located. The EMF meter used in this report is Extech 480836. It has an isotropic E-field sensor and converts the measurement value to H and S automatically using the standard far-field formulae for electromagnetic radiation, (A-4) and (A-5) [39]. That means H-field and **S** values are correct only in far-field case while E-field values measured are always correct. In this report we use the measured E-field strength to describe the EMF distribution since they are always correct. The EMF meter has a measurement frequency range of 50MHz-3.5GHz and does not measure EMF frequency itself. The E-field sensor inside the EMF meter can only measure EMF at certain frequencies: 900MHz, 1800MHz, and 2.7GHz. To measure EMF at other frequencies, we need to input a calibration factor to the meter. In the lab the dominate EMF is from wireless devices, and there are two Wi-Fi standards in the US, 02.11g/b at 2.4GHz and 802.11a at 5GHz. In this report, EMF frequency of 2.4GHz is assumed. When EMF strength is time variant, we should also measure its time dependence besides its spatial dependence. There are four measurement modes in Extech 480836 EMF meter: instantaneous value mode, average value mode (display average value in a short period of

time), maximum value mode (display maximum value since EMF meter is on) and average maximum value mode (display maximum of the average value since EMF meter is on). If EMF strength is changing rapidly, instantaneous value mode is used for time dependence measurement and maximum value mode is used for spatial dependence (distribution) measurement. If EMF strength stays steady we can simply use average value mode to get its distribution. In this report the distribution and time dependence of EMF strength inside and outside the lab are measured. From the distribution data, the dominate EMF sources can be positioned. After that, the characteristics of the EMF distribution in the lab are analyzed. In the end, the data are fitted to different theoretical radiation models by MATLAB.

II. EMF distribution outside the lab.

The top view of the building structure around lab ME-B1166 is shown in Fig.1. There is a Wi- Fi antenna in the corridor next to the lab which may contributes to the EMF level inside the lab. To measure the distribution of EMF right around the antenna, we can divide up the corridor into 4 ×35 grid (140 data points) then measure the EMF on every point. the EMF meter is tied to one side of a 130cm long wooden stick, and the other side of the stick is always on the ground. Since the time variance of EMF strength in the corridor is small, instantaneous value mode is used for measurement. The distribution of electric field on the corridor is presented in Figure A.2. In Figure A.2 we can see that EMF strength declines rapidly with the increase

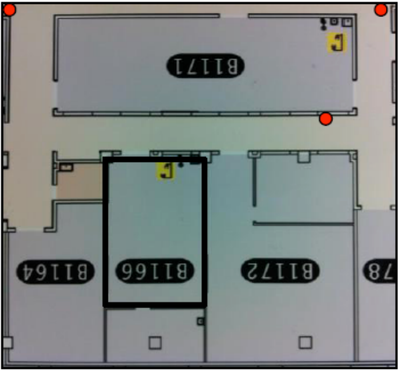

Figure A.1: WiFi Antenna locations (red dots) near B1166 of the Mechanical Engineering Building. Antennas are hung at wall about 9 feet above the floor.

of distance from the peak value point (just above the peak value point is the Wi-Fi antenna on the roof). In the vicinity of the lab, the EMF level is below 10mV/m and stable around 8mV/m. This illustrates that the Wi-Fi antenna contributes almost none to the EMF level inside the lab. Figure 2. The distribution of electric field on the corridor in 2D and 3D view. All the data are measured at the height of 130cm above floor.

III. EMS distribution inside the lab.

The EMF property inside the lab is much different from the outside region. When there are wireless devices ON in the lab such as laptops, EMF changes rapidly by time and it␣s difficult to obtain the instantaneous EMF strength distribution in the whole region inside the lab. In this case maximum value mode is used to measure the

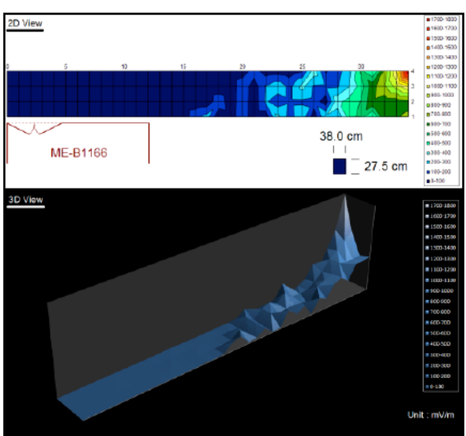

Figure A.2: EMF levels from WiFi Antenna locations. Antennas are hung at wall about 9 feet above the floor.

maximum value distribution (maximum in a certain period of measurement, e.g. 10 second) of EMF strength in the lab. The EMF time dependence will be discussed later. The lab can be divided into lab into 8×9 grid (72 data points). Electric field strength on every point is measured. The schematic view and EMF distribution inside the lab with MacBook Wi-Fi on/off are shown in Figure A.3. When Wi-Fi is off, the electric field inside the entire lab stays steady at 5.3-6.0 mV/m. When Wi-Fi is on, electric field reaches a peak of 500mV/m at the location of Caleb's MacBook; meanwhile the electric field level around measuring instruments in the lab is in the range of 10-30mV/m. Figure A.4 is the total EMF distribution both in the corridor and in the lab. In this figure the two dominate EMF source is located. Also, it clearly shows that the EMF is to a large extent determined by the wireless devices inside the

lab. What has discussed above is the planar EMF distribution at the height of 130cm above ground. To estimate the EMF strength at different heights in the lab, we can

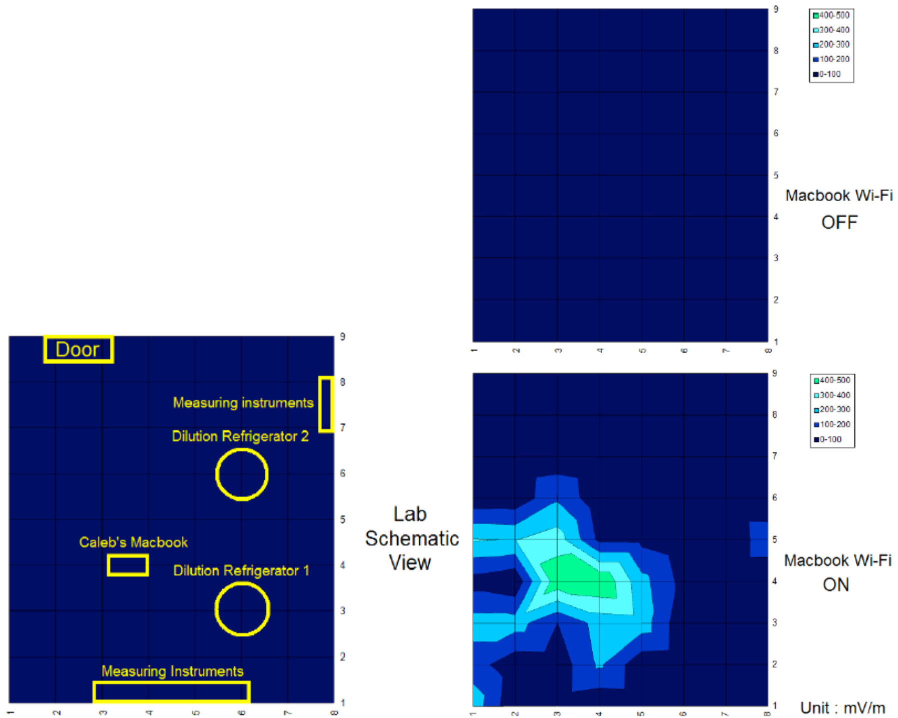

Figure A.3: The schematic view and distribution of electric field inside the lab with MacBook Wi-Fi on/off. When Wi-Fiis off, the electric field inside the lab stays steady at 5.3-6.0mV/m. All the data are measured at the height of 130cm above floor.

choose a particular location in ME lab and do the EMF measurement at different heights, as shown in Fig.5 (Wi-Fi OFF). The result illustrates that the EMF distribution does not changing too much with different heights with Wi-Fi OFF.

IV. EMF time dependence inside the lab.

When there are wireless devices in the lab, EMF changes rapidly by time, as discussed above. Instantaneous value mode of the EMF meter can be used for EMF

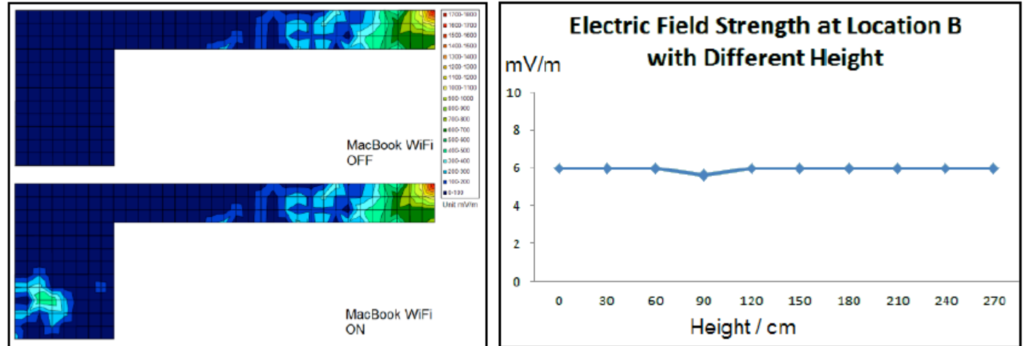

Figure A.4: (a)The total EMF distribution both in the corridor and in the lab, which shows that the lab EMF level is to a large extent determined by the wireless devices inside the lab.
(b) EMF strength at different heights in the lab with Wi-Fi OFF, measured at the location where the measuring instruments are placed in the lab with coordinates (4, 1) in (a).

time dependence measurement. The measurement results at two different locations are shown in Figure A.4. Location A is where the Caleb's MacBook is placed (the coordinates are (3, 4) in Figure A.4(a)) while Location B is where the measuring instruments are placed (the coordinates are (4, 1) in Figure A.4(a)). The distance between Location A and B is 180cm. Since the EMF meter Extech 480836 can only sample one discrete value at a time, there are some missing peaks in Fig.5 that are not been recorded. Figure A.4(b) shows that the EMF time dependence inside the lab follows a particular pattern: it jumps suddenly to the peak value then declines gradually until reaching the level of 6mV/m, which equals to the EMF level when the wireless devices are off. Because of the delay of the sensor head, the EMF meter is sensitive to a sudden rise but takes time to return to the normal value. That is why there are gradual declines in Figure A.4(b). Therefore, we can infer that what Figure A.4(b) shows are actually several

'impulses' instead of 'peaks'. In conclusion, the wireless devices emit EMF impulses every few seconds to stay connection with the antenna outside the lab. In the gaps between these impulses, the EMF level is the same as the case when Wi-Fi is off. In other words, the EMF distribution inside in lab is shifting between the patterns in the 2nd and 3rd diagram in Figure A.3 every few seconds.

V. Theoretical analysis of the EMF distribution

According to the classical electrodynamics [38],the radiation source can be regarded as a superposition of radiating dipole, radiating quadrupole and so on. Radiating dipole component is usually dominated in the far(radiation) zone. In the near zone ($r > 3\lambda$), the E-field of a single-frequency wave from radiating dipole ***p*** is:

$$\vec{E} = \left[3(\hat{r} \cdot \vec{p})\hat{r} - \vec{p})\right]\frac{1}{r^3} \tag{A-6}$$

In the far zone ($r < 3\lambda$), the E-field of a single-frequency wave from radiating dipole ***p*** is:

$$\vec{E} = k^2(\hat{r} \times \vec{p}) \times \hat{r}\,\frac{e^{ikr}}{r} \tag{A-7}$$

where $k = \dfrac{2\pi\nu}{c}$ and $\hat{r} = \dfrac{\vec{r}}{r}$.

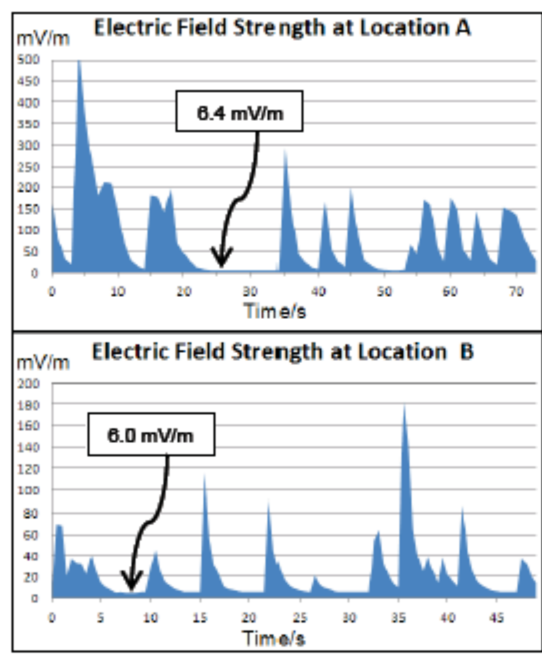

Figure A.5: Electric field time dependence at location A and B. The distance between A and B is 180_{cm} . All the data are measured at the height of 130_{cm} above the floor.

As we know, the frequency ν of the EMF emitted from the Wi-Fi antenna outside is a single frequency at 2.4GHz, then the wavelength $\lambda \sim 10_{cm}$. Thus, the EMF distribution around the antenna in the corridor is in the far zone, where the E-field is radially proportional to the inverse of distance to the antenna, (A-7). By using MATLAB toolbox we can fit the EMF distribution data measured to the theoretical E field expression in (A-7), as shown in Figure A.6. The correlation coefficient between the real EMF distribution and the theoretical EMF distribution is 0.9989, which proves the radiation pattern of the Wi-Fi antenna is analogous to that of a

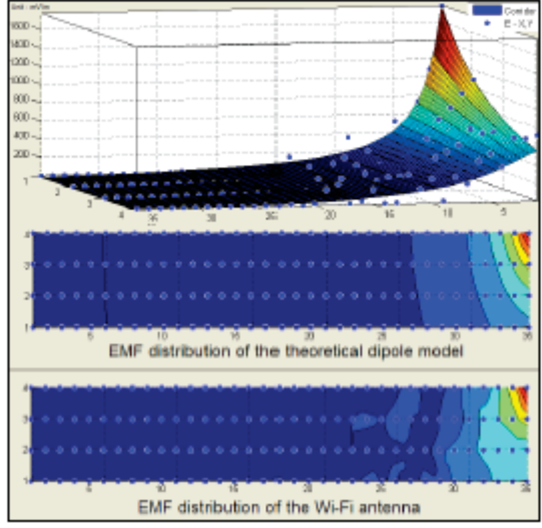

Fit Model	A*((x)^2+(y)^2)^(-0.5)+B
A	2635, (2612, 2658)
B	-87.25, (-90.26, -84.24)
R-square	0.9978

Figure A.6: Fitting of the EMF distribution data measured (blue dots) around the antenna to the theoretical radiating dipole E-field expression by MATLAB surface fitting toolbox. The correlation coefficient between the real EMF distribution and the theoretical EMF distribution is 0.9989.

single-frequency radiating dipole. In Figure A.6, it shows the MATLAB fitting toolbox output, including the expression of E-field and its parameters. As for the EMF distribution around wireless devices inside the lab, things are totally different. Firstly, from Fig.6 and the discussion above we know that the wireless devices, instead of giving 6.4 mV/m 6.0 mV/m out time invariant EMF waves, emit impulses of EMF, which contains a wide range of frequencies [40], and (A-7) for single-frequency wave no longer applies. In addition, there are several metals inside the lab which create metallic

boundary conditions and make the EMF distribution pattern irregular. After the data analysis of this case by MATLAB, we discovered that the EMF distribution in the lab does not fit the dipole EMF expression in (A-7), but follows the Gaussian function below, where A and σ are two parameters:

$$\vec{E} = Ae^{-\frac{r^2}{\sigma^2}} \tag{A-8}$$

The output of MATLAB fitting toolbox is shown in Figure A.7. Note that a new model, (A.9), is applied instead of (A-8) in the fitting process. Parameter B is introduced to cancel out the normal EMF level in the lab when Wi-Fi is OFF.

$$\vec{E} = Ae^{-\frac{r^2}{\sigma^2}} + B \tag{A-9}$$

In Figure A.7, the estimated value of B can be found as much as 9.5mV/m, which is close to the actual normal EMF level in the lab: 6.0mV/m. The correlation coefficient of 0.9745 tells that the Gaussian model does not fit very well to the data, for the irregularities in the original data, but we can still infer that it is the impulses emitted by the wireless devices, which contains a wide range of frequencies, that make the EMF distribution Gaussian-like.

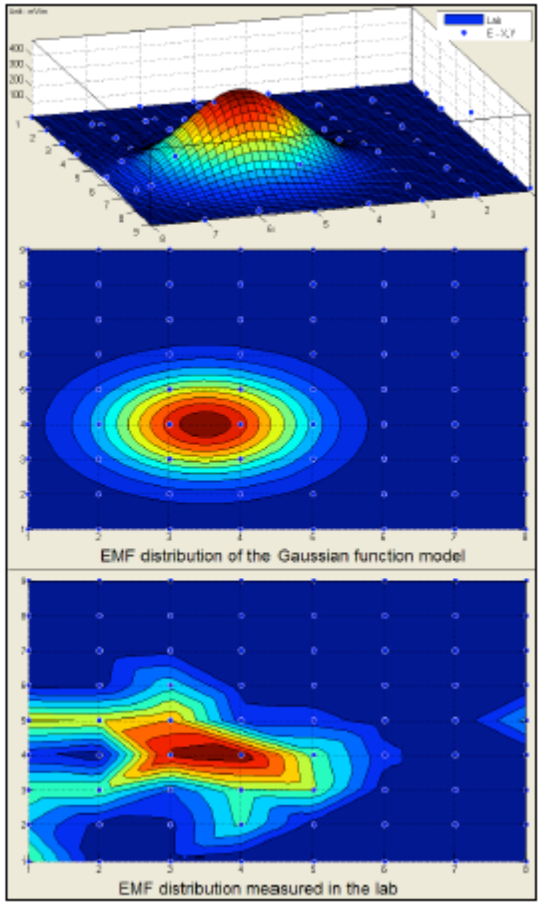

Fit Model	A*exp(-C*((x-3.5)^2+(y-4)^2))+B
A	525, (483.6, 566.4)
B	9.499, (1.922, 17.07)
C	0.4983, (0.4358, 0.5607)
R-square	0.9496

Figure A.7: Fitting of the EMF distribution data measured (blue dots) in the lab to the Gaussian distribution function (A-7) by MATLAB surface fitting toolbox. The correlation coefficient between the real EMF distribution and the theoretical EMF distribution is 0.9745

VI. Conclusion

The Wi-Fi antenna outside the lab contributes almost none to the EMF level inside the lab. The lab EMF level is to a large extent determined by the wireless devices inside the lab. The wireless devices emit an EMF impulse every few seconds to stay connection with the antenna outside the lab. In the gaps between impulses, the EMF level is the same as the case when Wi-Fi is off. The EMF emitted by the Wi-Fi antenna outside is single-frequency and the distribution of the EMF can be well fitted to the single frequency radiating dipole model. The EMF emitted by the wireless devices inside contains a wide range of frequencies and the distribution pattern of the EMF inside is Gaussian-like.

Acknowledgement

The EMF noise measurement and the following vibration measurement in Appendix B were done by visiting undergraduate student Chanyang Linghu from Tsinghua University, China. I thank his effort for performing measurement and writing report for our lab.

Appendix B

Vibration measurement in ME1166B

As the second part of the environmental noise measurement, the vibration level measurement result at different locations in the ME1166B is introduced. The vibration in ME1166B is mostly coming from the pump stations of the Dilution refrigerator, which is located in the separate room inside the ME116B. The room is called “pump room”, which is separated by a wall. In Figure B.1, top view of the ME1166B is shown. At the wall between the main room and the pump room, there is a window and through holes for pumping lines which connect the pumps and the fridge and the gas handling system on the table. Blue alphabet letters indicate locations of the measurement. A, B, C, and G are on the floor. E is on top of the wood plate, on which the fridge is sitting on. The wood plate is located about 2.5 feet above the floor. F is on top of the fridge, and H is on top of the optical table where the gas handling system is placed on. H is about 4 feet above the floor. C_{off} means measurement of C, when the pumps are off. We used Radio Frequency EMF strength Meter (EXTECHInstruments, Model:480836), ICP®Sensor Signal Conditioner (PCBPIEZOTRONICS, Model:482A21), and ICP®Accelerometer (PCB PIEZOTRONICS, Model : 393B04) and an oscilloscope. The sensor output voltage is

measured from the oscilloscope and converted to vibration acceleration using the calibration factor given from the manufacturer that is 103.3 mV/(m/s^2).

The results are shown in the Table B.1. Locations are listed in each row, and the second column is vibration acceleration data. As shown, H shows the strongest vibration acceleration. The reason is because there are several pumping lines connected to the pump and the distance between the table and the pump station is shortest among measured locations. So, it is strongly coupled to the pump station. On E and F, the vibration is significantly stronger than the floor. All the floor results, A, B, C, and G show similar values which is not significant. It looks that the floor of the ME1166B is very stable that there are not much environmental vibration.

The results suggest that it is best to anchor the fridge to the floor, or to a massive object such as a concrete block to minimize the vibration coupled from the environment. To de-couple the noise from the pump station, pumping lines may be sealed in sand boxes to damp down the noise.

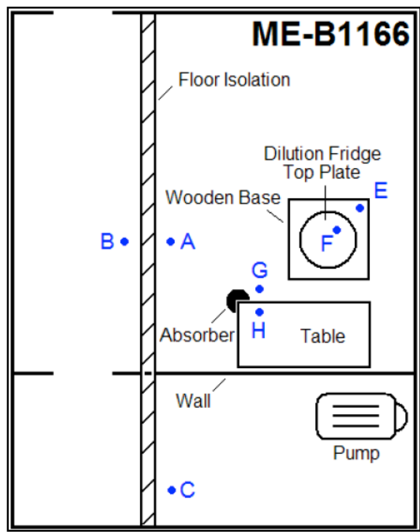

Figure B.1: Floor plan of ME1166B with vibration measurement locations (blue dots)

Point	Vibration Sensor Output Voltage (V_{p-p} : mV)	Vibration Acceleration (a_{p-p} : mm/s^2)	Vibration Displacement (d_{p-p} : nm)	Dominant Frequency (Hz)
A	**1.60**	**15.5**	**338**	30 60 360
B	**1.20**	**11.6**		24 60
C	**1.90**	**18.4**		60
C_{off}	**1.12**	**10.8**		Not exist.
E	**7.12**	**68.9**		230 1.85k
F	**5.20**	**50.3**		1.16k 2.52k
G	**1.52**	**14.7**		26 60
H	**42.8**	**414**		360 2. 63k

Table B.1: Vibration measurement results. The acceleration is obtained by dividing the voltage output by the calibration factor of 103.3mV/(m/s^2). The height of the blac rectangles ( ) under each frequency value shows the relative intensity of each frequency given by FFT.

Appendix C

Tunneling in a 1D rectangular barrier

One-dimensional (1D) rectangular barrier is the simplest model of a tunnel barrier. However, it is a very good approximation to many physical systems. Transmission coefficient of 1D rectangular barrier has been well studied, and can be found in many books [41]. One of example is shown in Figure 4.1, where V_0 is the height of the barrier and x is the direction of the wave propagation. As illustrated in Figure C.1,incoming wave and transmitted wave is shown. The electron wavefunction penetrates through the barrier even though classically it does not have enough energy to overcome the barrier. The transmission probability, T is calculated by solving the time-dependent 1D Schrodinger equations for the rectangular barrier, $V(x)$, where,

$$V(x) = V_0, \quad 0 < x < d \tag{C-1}$$

$$V(x) = 0, \quad x < 0, x > d. \tag{C-2}$$

To determine T, we construct the transfer matrix in each region, and combine them to find the total tunneling transmission.

Let's start at region 1&2 where there is the potential step up at $x = 0$.The electron wavefunctions are plane waves of the form $\exp(ikx)$, where k is the electron wavenumber.

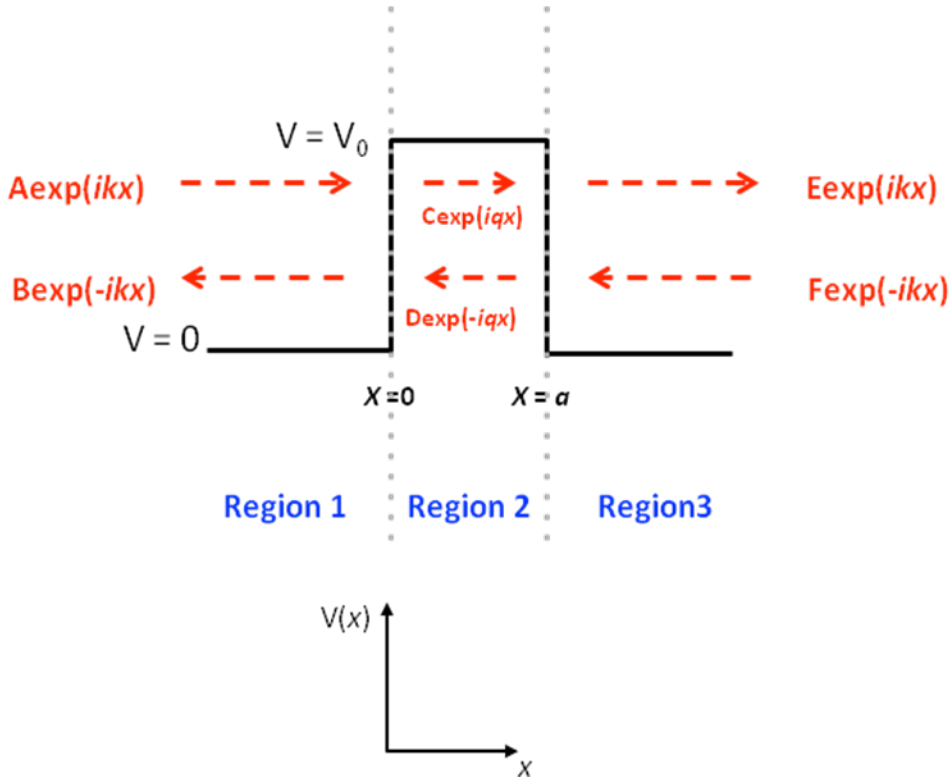

Figure C.1:A 1D rectangular potential barrier located at x = 0. The incoming wave and reflected wave in each region are shown as red arrows. V_0 is the height of the barrier and a is the length of the barrier.

$k = \sqrt{2m^* E/\hbar^2}$, while the wavenumber in region 2 is given $q = \sqrt{2m^*(E - V_0)/\hbar^2}$ .When $E > V_0$, the wavefunction in region 1 including the incoming wave and the reflected wave in region 1 is then:

$$\psi(x) = A\exp(ikx) + B\exp(-ikx) \tag{C-3}$$

where A and B represent the amplitudes of the incoming wave and the reflected wave respectably. Likewise, the wavefunction in region 2 is:

$$\psi(x) = C\exp(iqx) + D\exp(-iqx) \tag{C-4}$$

Sine the wavefunction, $\psi(x)$, and it's derivative, $d\psi(x)/dx$, must be continuous everywhere, we match the wavefunctions at x=0 to yield A+B = C+D, and k(A-B)=q(C-D). The resulting simultaneous equations are:

$$C = \frac{1}{2}(1 + k/q)A + \frac{1}{2}(1 - k/q)B \tag{C-5}$$

$$D = \frac{1}{2}(1 - k/q)A + \frac{1}{2}(1 + k/q)B \tag{C-6}$$

Assuming there is certainly an incoming electron traveling left to right in region 1, and there is no electron coming from right to left in region 2, A=1 and D=0. Since reflection gives an electron traveling right to left in region 1, B=r, where r is an amplitude of reflection. Similarly, C=t, where t is an amplitude of transmission. By substituting these

to (C-5) and (C-6), B = r = (k-q)/(k+q), C = t = 2k/(k+q). When E < V_0, q becomes iq, and the transmitted wave becomes a decaying exponential Cexp(-qx). These replacement result in B = r = (k-iq)/(k+iq), C = t = 2k/(k+iq).

In region 3&4, there isthe potential step down at $x = d$. The Same arguments as in the potential step up results in the simultaneous equations:

$$E = \frac{1}{2}(1 + q/k)C + \frac{1}{2}(1 - q/k)D \qquad \text{(C-7)}$$

$$F = \frac{1}{2}(1 - q/k)C + \frac{1}{2}(1 + q/k)D \qquad \text{(C-8)}$$

with C = 1, D = r = (q-k)/(q+k), E = t = 2q/(q+k). F = 0. When E < V_0, q becomes iq. This results in C = 1, D = r = (iq-k)/(iq+k), E = t = 2iq/(iq+k). F = 0.

We determined amplitudes of the reflected and transmitted waves at the potential steps with respect to the amplitude of the incoming wave. Now we construct the barrier using transfer matrix method. The advantage is that we can simply multiply the transfer matrix for each step to construct the full barrier. Starting from left to right, the matrix representation for equations (C-5) and (C-6) are:

$$\begin{pmatrix} C \\ D \end{pmatrix} = T^{(21)} \begin{pmatrix} A \\ B \end{pmatrix} \tag{C-9}$$

In tunneling regime (E < V_0),q becomes imaginary number. Replacing q to ip,$T^{(21)}$becomes :

$$T^{(21)} = \frac{1}{2ip} \begin{pmatrix} ip+k & ip-k \\ ip-k & ip+k \end{pmatrix} \equiv T(ip,k) \tag{C-10}$$

Similarly, the potential step down is represented as:

$$\begin{pmatrix} E \\ F \end{pmatrix} = T^{(32)} \begin{pmatrix} C \\ D \end{pmatrix} \tag{C-11}$$

where,

$$T^{(32)} = \frac{1}{2k} \begin{pmatrix} k+ip & k-ip \\ k-ip & k+ip \end{pmatrix} \equiv T(k,ip) \tag{C-12}$$

The full barrier is constructed by multiplying (C-10) and (C-12):

$$\begin{pmatrix} E \\ F \end{pmatrix} = T^{(32)} T^{(21)} \begin{pmatrix} A \\ B \end{pmatrix} = T^{(31)} \begin{pmatrix} A \\ B \end{pmatrix} \tag{C-13}$$

where$T^{(31)}$ represents the total transmission from region 1 to region 3. The reflection and transmission amplitudes r, and t are expressed in terms of elements from the transfer matrix $T^{(31)}$:

$$\begin{pmatrix} t \\ 0 \end{pmatrix} = T^{(31)} \begin{pmatrix} 1 \\ r \end{pmatrix} = \begin{pmatrix} T_{11}^{(31)} & T_{12}^{(31)} \\ T_{21}^{(31)} & T_{22}^{(31)} \end{pmatrix} \begin{pmatrix} 1 \\ r \end{pmatrix} \tag{C-14}$$

From (C-14), t and r can be given:

$$t = \frac{T_{11}T_{22} - T_{12}T_{21}}{T_{22}}, \qquad r = -\frac{T_{21}}{T_{22}} \tag{C-15}$$

So far, the developed transfer matrices are valid for a potential step at $x = 0$. In order to generalize it to a step at $x = a$, we only need to consider the phase shift from origin to the barrier location. The new matrix $T(a)$ from that at the origin $T(0)$ can be built in following three steps. First, translate the barrier from a to the origin by using new coordination $x' = x - a$. The phase of the incoming wave, $\exp(ikx)$ becomes $\exp(ikx')\exp(ika)$. This is just multiplying $\exp(ika)$ to the original phase term. The outgoing wave also be rewritten by multiplying $\exp(-ika)$ to the original phase term. In matrix notation, these are written as diagonal matrix with new phase terms. Second, now we can use $T(0)$ to get the amplitudes on the right. Finally, the barrier now be restored to d by reinstating $x = x' + a$. This process will introduce again the phase shift factors with

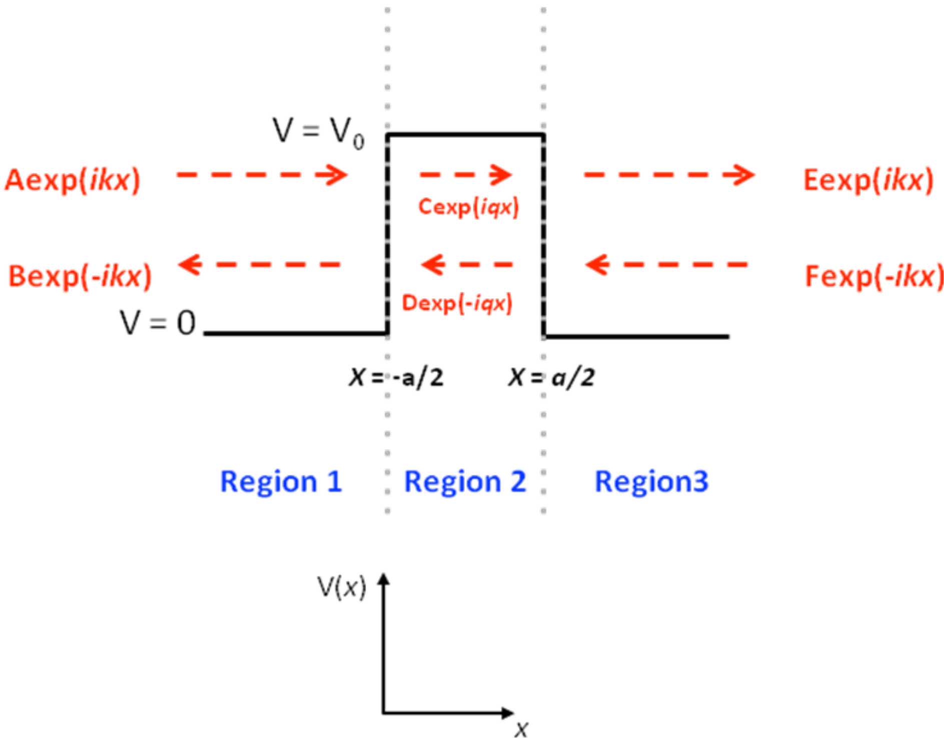

Figure C.2: A 1D rectangular potential barrier located at x = -a/2. The incoming wave and reflected wave in each region are shown as red arrows. V_0 is the height of the barrier and a is the length of the barrier.

opposite sign. The result will write $T(a)$:

$$T(a) = \begin{pmatrix} e^{-iqa} & 0 \\ 0 & e^{iqa} \end{pmatrix} T(0) \begin{pmatrix} e^{ika} & 0 \\ 0 & e^{-ika} \end{pmatrix} \tag{C-16}$$

Using (C-14) and (C-16), we can construct the *T* for a rectangular barrier shown in Figure C.2. For symmetricity, we consider a barrier with step up at x = -a/2, and step down at x = +a/2. At x = -a/2, the wavenumber changes from k to q, at x = +d/2, the wavenumber changes from q to k. The product of the two steps gives

$$\begin{aligned} T^{(31)} &= \begin{pmatrix} e^{-ika/2} & 0 \\ 0 & e^{ika/2} \end{pmatrix} T(k,q) \begin{pmatrix} e^{iqa/2} & 0 \\ 0 & e^{-iqa/2} \end{pmatrix} \\ &\times \begin{pmatrix} e^{iqa/2} & 0 \\ 0 & e^{-iqa/2} \end{pmatrix} T(q,k) \begin{pmatrix} e^{-ika/2} & 0 \\ 0 & e^{ika/2} \end{pmatrix} \end{aligned} \qquad \text{(C-17)}$$

Further multiplication gives

$$\begin{aligned} T^{(31)} &= \frac{1}{2kq} \begin{pmatrix} e^{-ika/2} & 0 \\ 0 & e^{ika/2} \end{pmatrix} \\ &\times \begin{pmatrix} 2kq\cos(qa) + i(k^2+q^2)\sin(qa) & -i(k^2-q^2)\sin(qa) \\ i(k^2-q^2)\sin(qa) & 2kq\cos(qa) - i(k^2+q^2)\sin(qa) \end{pmatrix} \\ &\times T(q,k) \begin{pmatrix} e^{-ika/2} & 0 \\ 0 & e^{ika/2} \end{pmatrix} \end{aligned} \qquad \text{(C-18)}$$

The middle matrix accounts for the barrier width, while the adjoining matrices on either side represent the phase factors which account for moving the barrier away from the origin. After final multiplications, we can get the elements of the *T* matrix:

$$T_{11}^{(31)} = \frac{2kq\cos(qa) + i(k^2 + q^2)\sin(qa)}{2kq} e^{-ika} \quad \text{(C-19)}$$

$$T_{12}^{(31)} = \frac{-i(k^2 - q^2)\sin(qa)}{2kq} \quad \text{(C-20)}$$

$$T_{21}^{(31)} = \frac{i(k^2 - q^2)\sin(qa)}{2kq} \quad \text{(C-21)}$$

$$T_{22}^{(31)} = \frac{2kq\cos(qa) - i(k^2 + q^2)\sin(qa)}{2kq} e^{ika} \quad \text{(C-22)}$$

From these elements, the transmission amplitude can be deduced.

$$t = \frac{T_{11}T_{22} - T_{12}T_{21}}{T_{22}} = \frac{1}{T_{22}} = \frac{2kq}{2kq\cos(qa) - i(k^2 + q^2)\sin(qa)} e^{-ika} \quad \text{(C-23)}$$

Since q is imaginary in tunneling regime ($E < V_0$), $\sin(qd) = \sin(ipd) = i\sinh(pd)$ where $p = \sqrt{2m^*(V_0 - E)/\hbar^2}$ and the transmission probability becomes

$$|t|^2 = \frac{4k^2 p^2}{4k^2 p^2 + (k^2 + p^2)\sinh^2(pa)} = \left[1 + \frac{V_0^{\,2}}{4E(V_0 - E)}\sinh^2(pa)\right]^{-1} \qquad \text{(C-24)}$$

Equation (C-23) shows that the tunneling probability depends on barrier height, V_0, electron energy, E, and length of the barrier, *a*. The tunneling probability decreases exponentially with the barrier length and the square root of the barrier height.

Appendix D

Table of parametric equations used in the models.

	Infinite Barrier		Finite Barrier	
Model name	**IC**	**IR**	**FC**	**FR**
Gate shape	Circular	Rectangular	Circular	Rectangular
w_0 & V_0	$4.88756e^{-8}+9.19836e^{-8}*V_g$		$E_a(V_g)= -0.00038 +7.2385e^{-6}*Exp[-V_g/0.05268]$ $E_a = V_0+E_0-E_F$	
r	$6.1241e^{-7} +1.5370e^{-6}*V_g$		$8.19751e^{-7} -4.39622e^{-7}*V_g$	
d	$5.54099e^{-8} -2.14822e^{-7}*V_g$		$-3.03305\ e^{-8} -2.1008\ e^{-7}*V_g$	

Bibliography

[1] S. M. Sze, *Semiconductor devices: Physics and technology*, John Wiley & Sons, 1985.

[2] http://en.wikipedia.org/wiki/Ivy_Bridge_(microarchitecture)

[3] Shor, P. W., *SIAM Journal on Scientific and Statistical Computing* 26: 1484. (1997).

[4] D.P. DiVincenzo, *Fortschr. phys*. 48, 771-783 (2000).

[5] Loss, D. and D.P. DiVincenzo, *Phys. Rev.A*, 57: 120. (1998).

[6] B.E. Kane, *Nature (London)* 393,133 (1998)

[7] J. R. Petta, A. C. Johnson, J. M. Taylor, E. A. Laird, A. Yacoby, M. D. Lukin, C. M. Marcus, M. P. Hanson, and A. C. Gossard, *Science* 309, 2180 (2005).

[8] J. M. Elzerman, R. Hanson, L. H. W. van Beveren, B. Witkamp, L. M. K. Vandersypen, and L. P. Kouwenhoven, *Nature (London)*430, 431 (2004).

[9] R. Hanson, L. H.Willems van Beveren, I. T. Vink, J. M. Elzerman, W. J. M. Naber, F. H. L. Koppens, L. P. Kouwenhoven, and L. M. K. Vandersypen, *Phys. Rev. Lett*. 94, 196802 (2005).

[10] K. MacLean, S.Amasha, I. P. Radu, D. M. Zumb¨uhl,M. A. Kastner, M. P. Hanson, and A. C. Gossard, *Phys. Rev. Lett*. 98, 036802 (2007).

[11] C. B. Simmons, et al*, Phys. Rev. Lett*. 106, 156804 (2011).

[12] M. Thalakulam, et al*, Phys. Rev. B*. 84, 045307 (2011).

[13] Zhan Shi, et al, *Phys. Rev. Lett.* 108, 140503 (2012).

[14] J. R. Prance, et al, *Phys. Rev. Lett.* 108, 046808 (2012).

[15] Mark Freisen Theory paper, to be apeared in the arxiv.

[16] http://www.nobelprize.org/nobel_prizes/physics/laureates/2000/

[17] E. Kasper, H. J. Herzog, and H. Kibbel, *Appl. Phys*. 8, 199 (1975).

[18] Fitzgerald E A, Xie Y-H, Green M L, Brasen D, Kortan A R, Michel J, Mii Y-J and Weir B E *Appl. Phys. Lett.* 59 811 (1991).

[19] LeGoues F K, Meyerson B S and Morar J F *Phys. Rev. Lett.* 66 2903 (1991).

[20] Hohnisch M, Herzog H-J and Schaffler F *J. Crystal Growth* 157 126 (1995).

[21] F. Schaffler, *Semicond. Sci. Technol*. 12, 1515 (1997).

[22] R. Dingle, H. L. Stormer, A. C. Gossard, and W. Wiegmann, *Appl. Phys. Lett*. 33, 665 (1978).

[23] Lu, T. M., Tsui, D., Lee, C.-H. & Liu, C. *Appl. Phys. Lett*., 94, 182102 (2009).

[24] Klitzing, K.; Dorda, G.; Pepper, M. *Phys. Rev. Lett.* 45 (6): 494–497 (1980).

[25] S. Das Sarma, and Frank Stern, *Phys. Rev. B.* 32 8442 (1985).

[26] F. Stern and S. E. Laux, *Appl. Phys. Lett*. 61, 1110

[27] P. T. Coleridge, *Phys. Rev. B.* 44 3793 (1991).

[28] K. Ismail, M. Arafa, K. L. Saenger, J. O. Chu, and B. S. Meyerson, *Appl. Phys. Lett.* 66 (9) 1077 (1994).

[29] S. F. Nelson and T. N. Jackson, *Appl. Phys. Lett*. 69, 3563 (1996)

[30]http://cdms.berkeley.edu/UCB/75fridge/inxsrc/dilution/index.html#1

[31] Mittal, A., Wheeler, R., Keller, M., Prober, D. and Sack, R. *Surf. Sci.* 362, 537

[32] Zieve, R., Prober, D. and Wheeler, R. *Phys. Rev. B* 57, 2443

[33]Martinis, J., Devoret, M. & Clarke, J. *phys. Rev. B* 35, 4682-4698(1987).

[34] Lukasheko, A. & Ustinov, A. V. *Rev. Sci. Instrum*. 79, 014701 (2008).

[35] J. R. Oppenheimer, Phys. Rev. 31, 66

[36] G. Gamow, Zeitchrift fur Physik 51, 204

[37] Esaki, L. *Physical Review*109 (2): 603 (1958).

[38] John David Jackson, *Classical Electrodynamics* (3rd Edition), Wiley, (1998).

[39] Extech Instruments Company, RF EMF Strength Meter User Guide, (2009).

[40] Constantine A. Balanis, *Antenna Theory:Analysis and Design* (3rd Edition), Wiley-Interscience, (2005).

[41] John H. Davies, The physics of low dimensional semiconductors: an introduction, Cambridge university press, (2005)

[42] M. Field, C. G. Smith, M. Pepper, D. A. Ritchie, J. E. F. Frost, G. A. C. Jones, and D. G. Hasko, *Phys. Rev. Lett*. 70, 1311–1314 (1993)

[43] http://goldbook.iupac.org/A00446.html